5. IMPURITY CONTROL SYSTEM

Farrokh Najmabadi
Steven P. Grotz
Shahram Sharafat
Eric L. Vold

Patrick I. H. Cooke
Mohammad Z. Hasan
Don Steiner

Michael J. Gouge
Tomoaki Kunugi
Mark E. Valenti
Clement P. C. Wong

Contents

5. IMPURITY CONTROL SYSTEM

5.1. INTRODUCTION

The design of in-vessel components (divertor plate, limiter, first wall) is probably the most critical engineering and physics issue for all fusion reactors. The key problem is to dispose of the steady-state plasma power (alpha-particle and current drive) while maintaining acceptable heat fluxes and erosion rates on all components. Evidence shows that this can be accomplished with a divertor operating in the high-recycling regime that exhibits a high density and low temperature at the divertor target. Therefore, a double-null poloidal divertor operating in the high-recycling regime has been chosen for the ARIES-I reactor.

The high-recycling regime has been experimentally observed in several devices (*e.g.*, D-III-D, ASDEX, and JET). For modeling the ARIES-I edge plasma, two 2-D edge-plasma computer codes, BRAAMS [1] and EPIC [2], were used. Results from these codes were compared previously, by simulating the ASDEX tokamak divertor experiment, and were found to be in reasonably good agreement with those from that experimental plasma regime [3]. It should be noted, however, that large uncertainty exists in the results of these codes when applied to reactor-relevant regimes. To ensure consistency with 0- and 1-D BALDUR core-plasma simulations, the edge-plasma analyses use the particle and heat fluxes at the separatrix as inputs. The computational analyses indicate that the resultant plasma density at the separatrix would be high ($\sim 10^{20}$ m^{-3}) and a high-recycling divertor regime is formed with a peak heat flux of $\sim$4.5 MW/m^2 and a rather low plasma temperature of 10 to 20 eV at the divertor target. Furthermore, assuming that the ratio of α-particle to electron density is similar to that of the core plasma, calculations show that effective ash exhaust would be achieved. Results of the ARIES-I simulations of edge-plasma parameters and particle exhaust rates are described in Sec. 5.2. The sputtering erosion of ARIES-I in-vessel components is discussed in Sec. 5.3.

The two main engineering design issues for the divertor system are to achieve heat loadings on the divertor target plate that do not exceed the maximum acceptable level and to simultaneously ensure that the sputtering erosion rate does not lead to an early failure of the component. These two aims tend to conflict because the high heat loadings, which inevitably occur on the divertor target, require the use of thin structures to minimize temperature differences and thermal stresses, while a thick structure is necessary to give a

long life against erosion. The ARIES-I divertor plate is made of a bank of silicon-carbide (SiC) composite tubes. The plasma-facing side of the tube bank has a 2-mm-thick, plasma-sprayed tungsten coating. Tungsten was chosen for the coating material because of its low erosion rate and excellent compatibility with SiC. The target plate is inclined with respect to the flux surface (at a 10° angle at the strike point) to limit the peak heat flux on the divertor plate to 4.5 MW/m^2. Because of large uncertainty in edge-plasma parameters and because the heat-flux estimate given above does not account for such factors as toroidal asymmetries or target misalignment, an engineering safety margin of $\sim$2 was chosen as the divertor design goal (*i.e.*, localized heat fluxes twice as large as the estimated value can be handled). The coolant is helium and the inlet and exit temperatures are, respectively, 350 and 650 °C, the same as those of the blanket coolant circuit. As a result, the divertor power is recovered by the main thermal-conversion cycle at a gross efficiency of 49%. The required circulator power for the divertor cooling circuit is 35 MWe and represents 12% of the recovered thermal power from the divertor coolant circuit. The thermostructural design of the divertor target plate, including finite-element analyses, are given in Sec. 5.4.

Thermal response of the ARIES-I divertor plate to plasma disruption and fluid dynamics of the melt layer have been analyzed numerically using 2-D codes (Sec. 5.5). A simple model is used for vapor shielding, and only the surface tension and buoyancy forces are used in modeling the fluid dynamics of the melt layer. With a vapor shield, the total evaporation of the tungsten coating of the divertor plate is about 48 μm and the coating is, therefore, expected to withstand about 20 to 40 disruptions before requiring divertor plate replacement or recoating.

ARIES-I utilizes an advanced, high-speed pellet-injection system to achieve and maintain ignited plasmas. Three pellet injectors are provided. For ramp-up to ignition, a moderate-velocity (1 to 1.5 km/s) single-stage pneumatic injector with high reliability and a high-velocity (4 to 5 km/s) two-stage pneumatic pellet injector using frozen hydrogenic pellets encased in sabots are proposed. For the steady-state burn phase, a continuous, single-stage pneumatic injector is utilized, which will provide a flexible fueling source beyond the edge region to aid in decoupling the edge region (constrained by divertor requirements) from the high-temperature burning plasma. Pellet-injection-system design issues such as performance, neutron activation of injector components, maintenance, design of the pellet-injection vacuum line, gas loads to the reprocessing system, and equipment layout are discussed in Sec. 5.6.

A summary and R&D directions for the impurity-control/particle-exhaust system are given in Sec. 5.7.

5.2. EDGE-PLASMA SIMULATIONS

5.2.1. Computational Models

In the high-recycling divertor regime, the plasma density in front of the divertor target is increased through extensive neutral recycling in a region localized in front of the divertor target plate. The plasma pressure balance along the field line then results in a reduction in the plasma temperature at the target plate. Because the plasma flow to the target plate along the field lines is impeded by the recycling, the plasma particle and heat fluxes tend to diffuse radially, decreasing the peak heat flux on the divertor plate. Basically, a high plasma density in the scrape-off layer is a prerequisite for achieving a high-recycling regime. The high-recycling regime has been experimentally observed in several devices (*e.g.*, D-III-D, ASDEX, and JET). For modeling the ARIES-I edge plasma, two two-dimensional (2-D) edge-plasma computer codes, BRAAMS [1] and EPIC [2], were used. Results from these codes were compared previously, by simulating the ASDEX tokamak divertor experiment, and were found to be in reasonably good agreement with those from that experimental plasma regime [3]. It should be noted, however, that large uncertainty exists in the results of these codes when applied to reactor-relevant regimes.

Most edge-plasma transport simulations are based on a set of fluid equations that were derived by Braginskii [4]. In general, a set of fluid equations for plasma density, momentum, and electron and ion temperatures are coupled with a model for neutral particle transport. Edge-plasma simulation codes use different neutral models. The B2 code used for the ARIES-I analysis uses an analytic form, while EPIC uses a diffusive neutral-transport model. The plasma transport equations are augmented by expressions for anomalous particle, heat, and momentum diffusion perpendicular to the flux surface. For example, the anomalous radial particle flux, Γ_{an}, is defined in terms of anomalous coefficients for diffusion, D_a, and for advection, V_a,

$$\Gamma_{an} \equiv n V_a - D_a \nabla_r n \,. \tag{5.2-1}$$

The values of the anomalous transport coefficients, D_a and V_a, are found by comparing the experimental observation for edge-plasma profiles with code predictions. Because the experimental data on edge-plasma parameters are rather limited, the values of these anomalous coefficients have a broad range (D_a values between 0.1 to 10 m^2/s have been reported). For the ARIES-I edge-plasma analysis, we have used typical medium values for the anomalous transport coefficients: particle diffusivity of $D_a = 1$ m^2/s, a radial inward pinch velocity of $V_a = -20$ m/s, and ion and electron heat diffusivities of, respectively, $\chi_e = 4$ and $\chi_i = 1$ m^2/s.

A schematic of the divertor plate is given in Fig. 5.2-1(A). Both B2 and EPIC solve the edge-plasma transport equations in the poloidal plane, assuming toroidal symmetry. The B2 code uses analytic transforms which map the magnetic geometry into a rectangular domain. The advantage of this treatment is that the analytic functions are defined as an orthogonal set so that a very fine mesh can be generated easily. However, the analytical fitting functions only approximate the poloidal flux surfaces and the fitting parameters should be chosen carefully so that the magnetic shear, B_θ/B_{tot}, is consistent with the actual magnetohydrodynamic (MHD) equilibrium solution.

The EPIC grid geometry, shown in Fig. 5.2-1(B) is generated numerically from the actual ARIES-I MHD equilibrium data (Sec. 3). The advantage of this geometry generation is that the actual magnetic geometry data are used so that the poloidal flux surfaces and the magnetic shear are consistent with the real equilibrium solution. At present, EPIC does not include internal MHD equilibrium solvers and uses output from an MHD equilibrium code (*i.e.,* NEQ). Therefore, the grid resolution is proportional to the density of the magnetic-flux output data, and the grids are typically coarser than with the analytic grid generator used for the B2 code. However, the numerical grids are fully self-consistent and, therefore, likely to be more accurate on the coarse scale.

5.2.2. Simulation Results

For ARIES-I edge-plasma simulations, only the outboard scrape-off layer was modeled. The target is assumed to be normal to the poloidal flux surfaces and the power to the target is then corrected for the target inclination angle, assuming that the plasma solution does not change appreciably with the poloidally inclined target. In order to ensure self-consistency with the BALDUR core-plasma transport analyses, the particle and heat fluxes from the core (respectively, $10^{19}/m^2$-s and 0.4 MW/m^2) are used as the boundary condition (rather than upstream density and temperature). Both codes assume that 20% of the heat flux across the separatrix is in the ion channel and that the remaining 80% is in the electron channel. The heat flux across the separatrix accounts for the synchrotron and bremsstrahlung losses from the core plasma. In order to be conservative, no credit is taken for any radiation in the scrape-off layer and/or by impurity line radiation in the plasma. Additional radiation losses would reduce the heat flux on the divertor plate. The major input parameters for the ARIES-I edge-plasma simulations are given in Table 5.2-I.

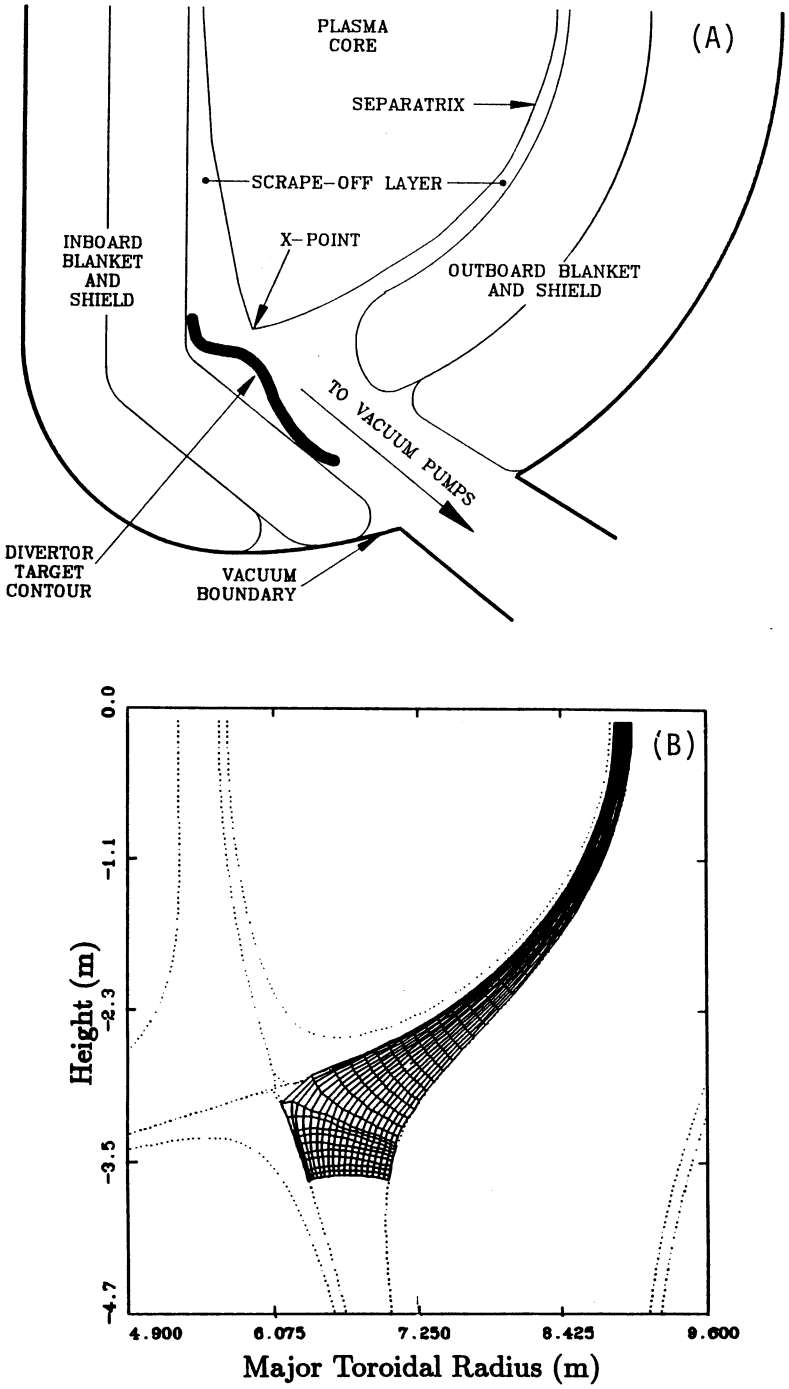

Figure 5.2-1. (A) Schematic of the ARIES-I divertor layout. (B) The computational grid used by EPIC edge-plasma simulation code.

Table 5.2-I.
Major Input Parameters for ARIES-I Edge-Plasma Simulations

Plasma major radius (m)	6.75
Plasma half width (m)	1.50
Plasma vertical elongation	1.8
Poloidal distance (m)	
Mid-plane to $\times$-point	4.2
$\times$-point to target	0.6
Total power into edge plasma (MW)	242
Heat flux into edge plasma (MW/m^2)	0.4
Fraction of heat flux in ion channel	0.2
Particle flux into edge plasma ($10^{19}/m^2$-s)	1
Particle diffusion coefficient (m^2/s)	1
Ion thermal diffusivity (m^2/s)	1
Electron thermal diffusivity (m^2/s)	4
Anomalous advective velocity (m/s)	-20

5.2.2.1. Results from the B2 code

The B2 code is started from a "constant-field" initial condition of $n = 10^{20}$ m^{-3} and $T_i = T_e = 10$ eV. The solution evolves for 600 iterations afterwhich the solution convergence slows; this is defined to be the steady-state solution. Attempts to evolve the solution longer than this show that the solution does diverge slowly. It is not clear if this long-term divergence is only due to numerical errors.

The estimated plasma conditions at the divertor target from the B2 code depend upon a recycle parameter, R, which must be specified independently. Here, R is defined as the number of neutrals returned from the divertor target per incident plasma ion. In principle, all of ions incident on the divertor plate should be returned as neutral. But, the simple analytical neutral model in B2 requires a range of 0.9 to 0.99 for R. This range of R was, therefore, examined parametrically. The results of the B2 simulations for the peak heat flux and plasma temperature at the divertor target are shown in Fig. 5.2-2. These parametric results show that the divertor plasma parameters are sensitive to the value of R in this range.

As R increases, the upstream separatrix density also increases. The value of $R = 0.98$ corresponds to an upstream electron density of 10^{20} m^{-3}. This upstream density was calculated by EPIC using its self-consistent neutral-transport model. This value of R is, therefore, adopted as the reference case. The change in the heat flux along the divertor plate for this solution is shown in Fig 5.2-3. The characteristics of this solution are given in Table 5.2-II. It should be noted that parallel plasma flow was found to be mildly reversed in a large region near the separatrix.

5.2.2.2. Results from the EPIC code

The EPIC code is run from constant-field initial conditions of low density ($< 10^{19}$ m^{-3}) and low temperature ($T_i = 4$ eV, $T_e = 14$ eV). It was found necessary to start the simulation with a large, anomalous diffusive particle flux ($\geq 10^{21}$ m^{-2}s^{-1}) to "fill up" the edge plasma, and to allow recycling at the target to evolve and a high plasma density to build at the divertor target region. As this solution approached convergence, the particle flux is cut back to the desired steady-state flux rate (10^{19} m^{-2}s^{-1}) while simultaneously an anomalous, inward pinch velocity, $V_a = -20$ m/s, is turned on. Convergence was defined as the situation when the maximum norm was less than the specified tolerance of 2×10^{-4}. It should be noted that, similar to B2 simulations, EPIC simulations also diverge if simulations continue for a considerably longer time. Further research is needed

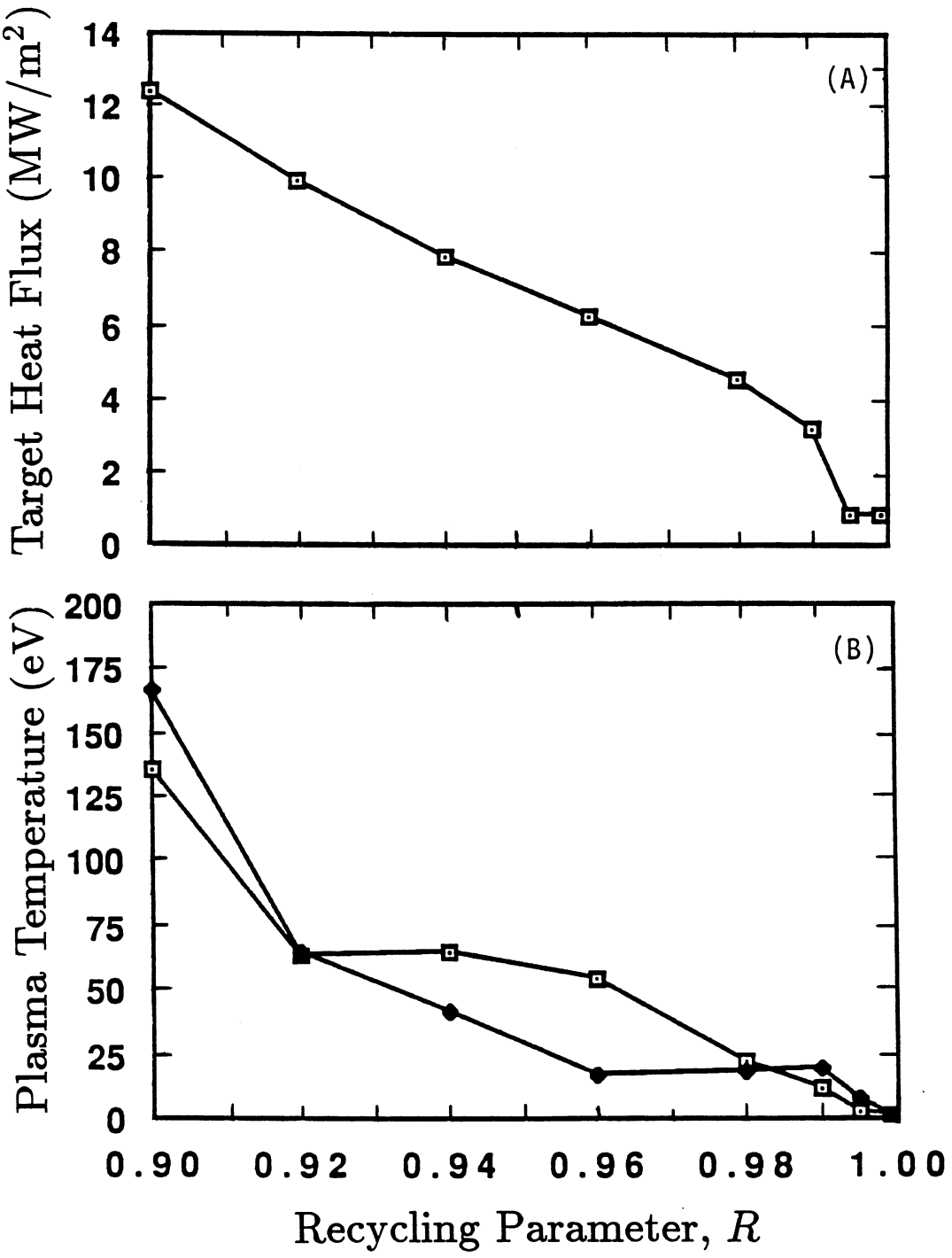

Figure 5.2-2. Results of the B2 simulations of the ARIES-I edge plasma as a function of the recycling parameter, R: (A) peak electron (open squares) and ion (filled squares) temperatures and (B) peak heat flux (on the divertor target).

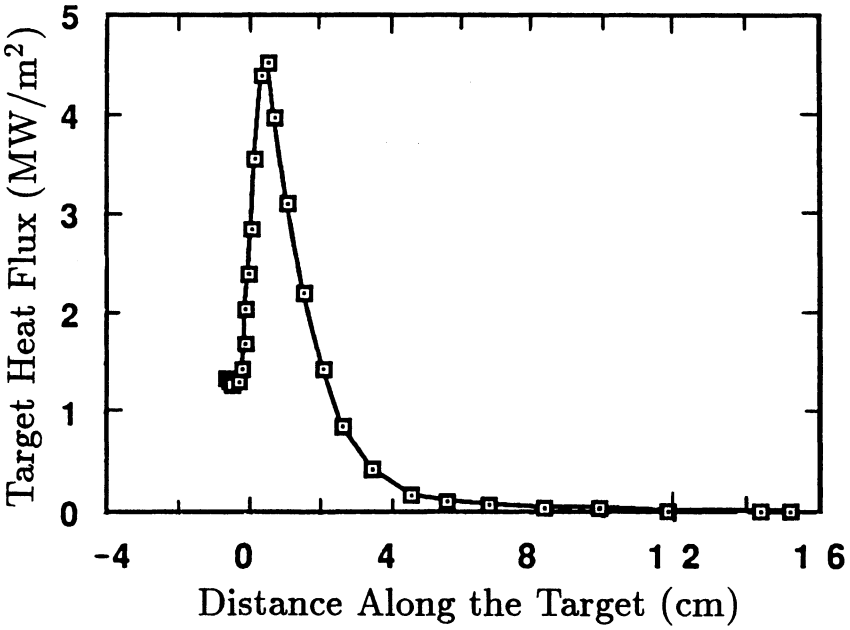

Figure 5.2-3. The heat flux along the ARIES-I divertor plate (reference B2 code results with $R = 0.98$) for a target perpendicular to the flux surface (position 0 indicates the strike point). The heat flux is corrected for a 10° inclination of the target plate.

to determine if this divergence is due to numerical problems or if it signifies a physics phenomena.

The nominal EPIC steady-state solutions are shown in Figs. 5.2-4 and 5.2-5 for the plasma density and electron temperature. Corresponding radial profiles at three poloidal locations (mid-plane, near the ×-point, and at the target) are also shown (the radial scale corresponds to the position of the flux surface when mapped into the divertor target). These results are compared to B2 simulation results in Table 5.2-II. Contours of neutral density for the EPIC solution are shown in Fig. 5.2-6, which shows that the neutrals are confined in the region in front of the divertor plate and do not enter the core plasma.

5.2.2.3. Discussion

Results of the calculations by the B2 and EPIC codes are compared in Table 5.2-II. It should be noted that the computational grid used for the B2 calculations only approximately matches the ARIES-I flux surfaces, and some of the differences between the results of the two codes can be attributed to the use of different grids.

Table 5.2-II.
ARIES-I Edge-Plasma Parameters

	B2 Results[a]	EPIC Results
Separatrix		
Plasma density (10^{20} m^{-3})	0.9 – 1.3	1
Ion temperature (eV)	520	300
Electron temperature (eV)	260	220
Mid-plane scrape-off layer		
Density e-folding length (cm)	4	5
Power e-folding length (cm)	2	2
First-wall plasma density (10^{18} m^{-3})	1.2	3
First-wall plasma temperature (eV)	25 – 30	20 – 25
Divertor plasma (peak values)		
Ion temperature (eV)	11	22
Electron temperature (eV)	22	25
Plasma density (10^{20} m^{-3})	9	8
Particle flux (10^{23}/m^2-s)	2.2	2.6
Heat flux (MW/m^2)	4.5	3.0

[a] For recycling parameter, $R = 0.98$.

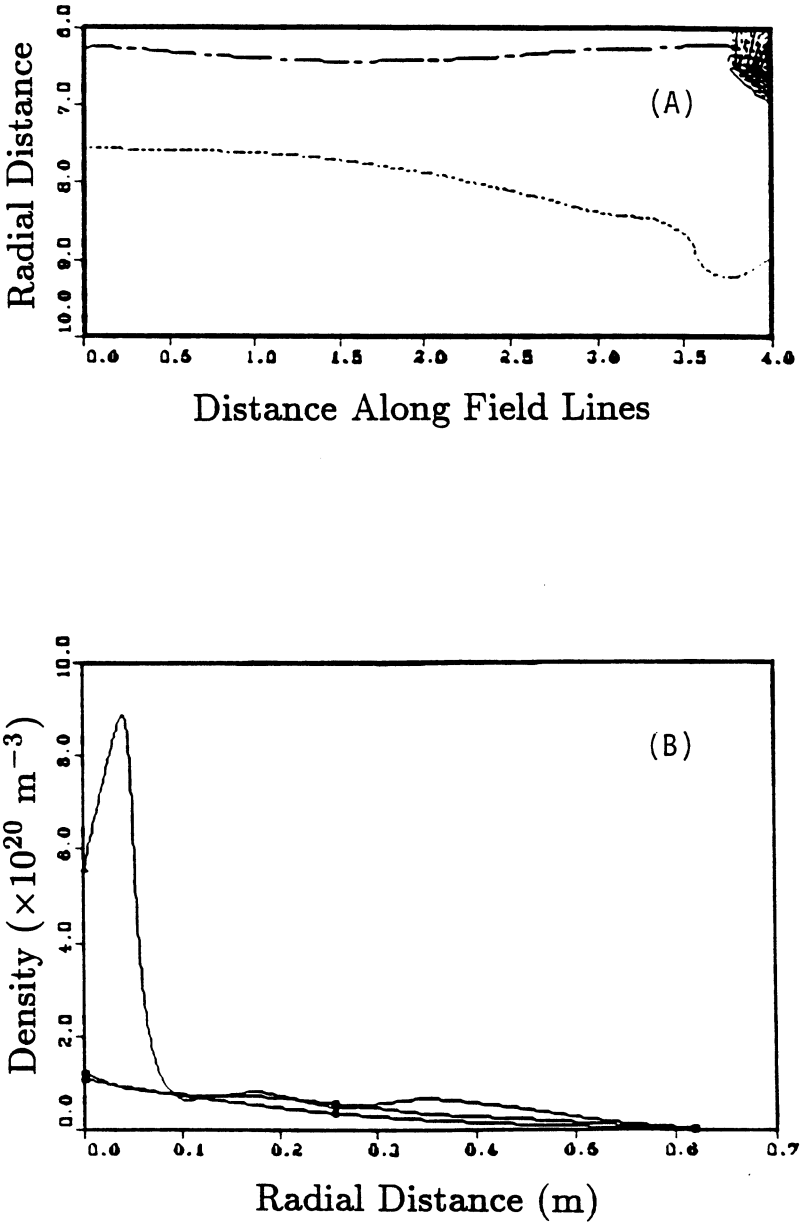

Figure 5.2-4. EPIC simulations of the ARIES-I edge plasma: (A) contours of plasma density and (B) radial density profiles at three poloidal locations: mid-plane, near the $\times$-point, and at the divertor target (the radial scale corresponds to the position of the flux surface when mapped into the divertor target).

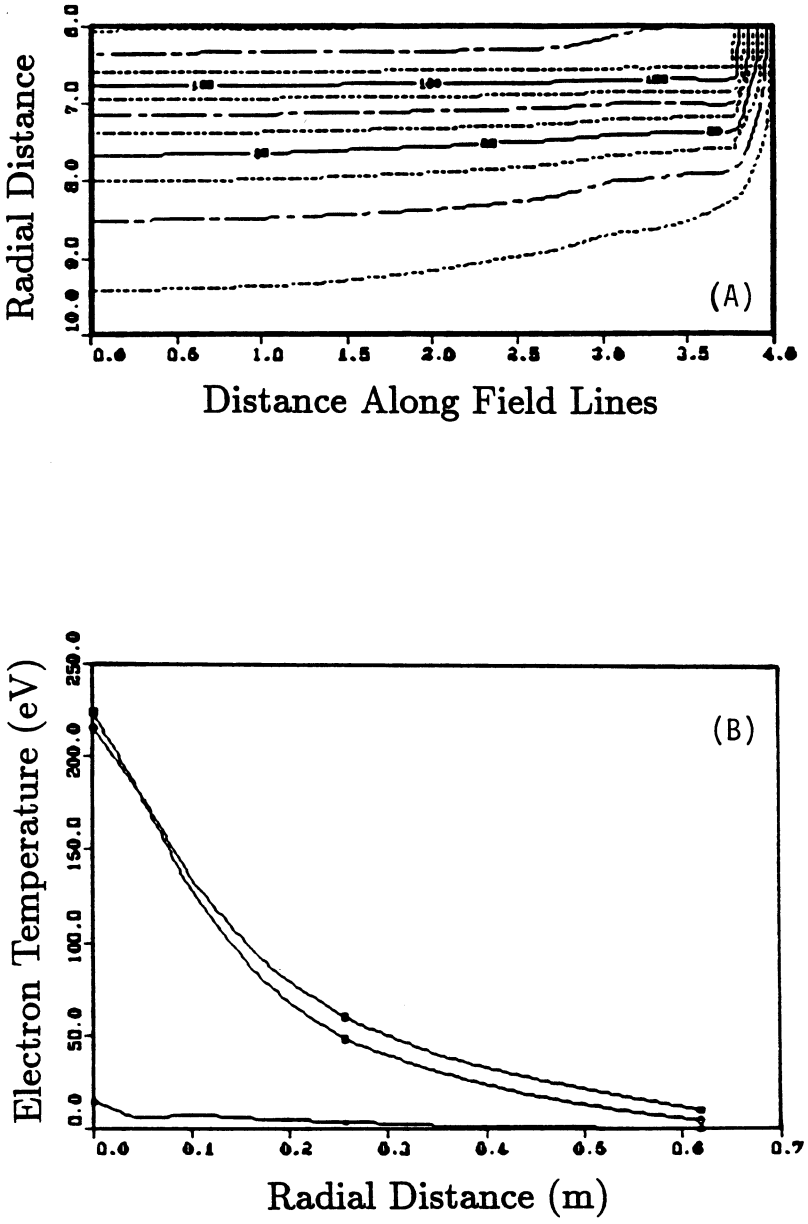

Figure 5.2-5. EPIC simulations of ARIES-I edge plasma: (A) contours of electron temperature and (B) radial temperature profiles at three poloidal locations: mid-plane, near the $\times$-point, and at the divertor target (the radial scale corresponds to the position of the flux surface when mapped into the divertor target).

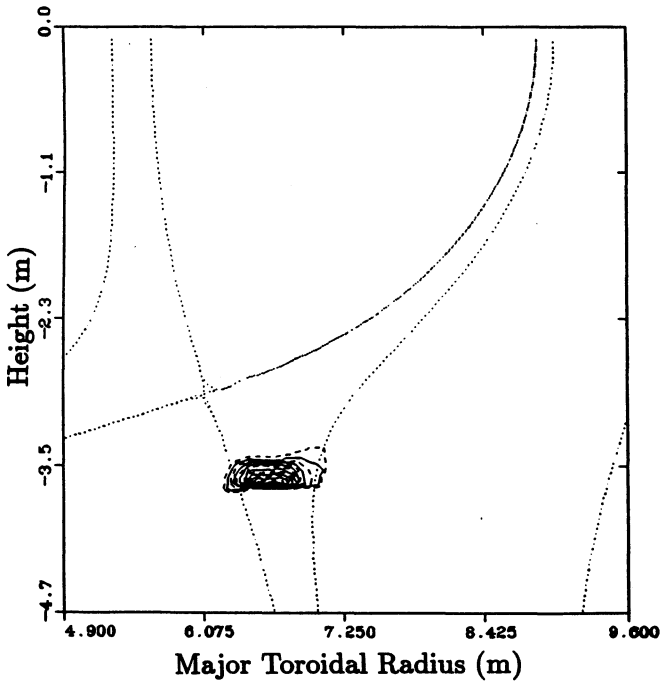

Figure 5.2-6. EPIC Simulations of the ARIES-I edge plasma: contours of neutral density showing strong recycling near the divertor target and negligible leakage to the core plasma.

Both codes predict a high separatrix density of $\sim 10^{20}$ m^{-3}. The power and particle e-folding lengths are also in good agreement, emphasizing the need to include the anomalous inward pinch term to achieve realistic solutions. The predicted plasma temperatures at the first wall are also comparable between the codes. The plasma densities differ by a factor of three, probably because of differences in the boundary conditions assumed, and with the value being sensitive to the inward advective velocity assumed. The B2 code shows a large poloidal gradient along the separatrix, increasing from the mid-plane towards the $\times$-point, which is not seen in the EPIC solution. The separatrix plasma shows large differences in ion temperature between the B2 and EPIC codes. These differences are also probably because of the way the two codes handle the boundary conditions at the separatrix.

At the divertor target, both codes show a high-recycling regime with peak divertor plasma densities of $\sim 10^{21}$ m^{-3} in a localized region near the separatrix-target strike point, where the peak electron temperatures are about 25 eV. Larger differences in the ion temperatures, however, are obtained (11 and 22 eV for, respectively, the B2 and EPIC codes). Furthermore, the EPIC solution shows an anomalous second peak in the

ion temperature ($\sim$100 eV) away from the separatrix in the middle of the divertor target. This second peak is the result of the intense recycling and neutral plasma interactions (especially in the momentum terms) which become dominant over the ion-electron equilibration terms and allow a large difference between the ion and electron temperatures. Even if this peak is real, its contribution to target sputtering is not large since, at that position, the electron temperature (and the sheath potential) is small.

Even though the values of the peak plasma density in the recycling zone are in agreement between B2 and EPIC, the B2 code shows an anomalous result. The plasma density increases along the divertor target from the separatrix inward to the private flux region to a peak value at the private flux boundary of 7×10^{21} m^{-3}, or an order of magnitude higher than in the area expected to exhibit the peak recycling (near the separatrix-target intercept). This is probably caused by the boundary condition imposed on the private flux region and by the limitation of the recycling neutral model which does not allow neutral transport across magnetic flux lines.

The estimates of the peak heat load on the divertor target plate differ. The EPIC estimate (3 MW/m^2) is lower than that of the B2 code (4.5 MW/m^2). Consistently, EPIC estimates a longer radial e-folding length for power in front of the divertor plate. This difference is believed to be due to the different neutral models used: the B2 code neutrals are recycled on the same field line while the EPIC neutral-diffusion model allows a realistic cross-field flux of particles, and with them, momentum and energy. Even though the lower heat loads of EPIC are probably more realistic, the heat flux predictions of the B2 code were used in the divertor thermostructural analyses in order to be conservative.

5.2.3. Particle Exhaust and Pumping

In order to maintain a steady plasma burn, the fusion α-particle ash should be exhausted from the system. For ARIES-I, the α-particle production (and removal) rate is $\dot{\phi}_\alpha \approx 6.8 \times 10^{20}$/s. Similar transport and recycling is assumed for α-particle and DT fuel ions, resulting in a required particle (ion) exhaust rate of $\sim 7 \times 10^{21}$/s. The EPIC simulations result in an average neutral density of 2×10^{19} m^{-3} (pressure of 20 mtorr) in front of the pumping ducts. The required effective pumping rate is, therefore, 350 m^3/s.

The ARIES-I reactor has 16 pumping ducts (only the lower divertor plates are pumped). The estimated pressure of 20 mtorr is sufficiently high that pumping speed requirements are not excessive. At these pressures, the gas flow is in the transition range between molecular and viscous flow. Using standard prescriptions for vacuum-pumping

ducts [5], the net conductance of each duct is estimated to be ~250 m^3/s. Therefore, the vacuum pumping speed required at each duct location is ~25 m^3/s. This pumping speed is estimated to be enough for pumping down the plasma chamber to a base pressure of 10^{-8} torr prior to the plasma start-up.

Turbo-molecular pumps are proposed for the ARIES-I reactor. Using these pumps (instead of cryogenic pumps) reduces the tritium inventory in the plasma exhaust system considerably. Although a metallic turbo-molecular pump has to be shielded from the magnetic field, a ceramic pump doesn't require shielding. These ceramic pumps are being developed in Japan, but the pump size is small at present [6].

5.3. EROSION

The interaction of the plasma and the wall surface is a critical issue for reactor design. The sputtering and erosion of the wall by plasma ion bombardment must be acceptably small to provide a practical lifetime for the wall material. The erosion rate, S (thickness eroded per unit time), is given by

$$S = Y \Gamma \frac{A_w}{\rho_{sg}}, \tag{5.3-1}$$

where Y is the sputtering yield (atoms sputtered per incident ion), Γ is the plasma ion flux, and A_w and ρ_{sg} are, respectively, the atomic mass number and the specific gravity of the wall material.

Both the yield and the flux are energy dependent and vary considerably over the expected range of ion energies. To account for this energy dependence, it is convenient to define $\Gamma(E) = \Gamma f(E)$, where $f(E)$ includes the energy dependence of the flux $[\int_0^\infty f(E)dE = 1]$. Then,

$$S = \frac{A_w}{\rho_{sg}} \Gamma \int_0^\infty Y(E) f(E) dE . \tag{5.3-2}$$

For ARIES-I analyses, the sputtering yield data is taken from Matsunami *et al.* [7] where an empirical formulation is developed to fit a wide data base. The energy dependence of the flux is taken to be a shifted Maxwellian distribution,

$$f(E) \propto E^{1/2} e^{-(E-\Delta E/T)}, \tag{5.3-3}$$

where T is the ion temperature at the material boundary. The energy shift, ΔE, is given by

$$\Delta E = \frac{1}{2} m_i C_s^2 + \gamma_e Z T_e , \tag{5.3-4}$$

where the first term accounts for the acceleration of an ion with mass, m_i, and atomic number, Z, to the sound speed, C_s; the second term is due to the acceleration by the sheath potential. The sheath transmission factor, γ_e, is taken to be

$$\gamma_e = 0.37 ln \left(\frac{m_{DT}}{m_e} \frac{T_e}{T_i} \right) , \tag{5.3-5}$$

where $m_{DT} = 2.5$ amu is the average mass of ion species. The sheath and presheath energy shift is assumed to apply to all wall surfaces.

The ion energies and fluxes are taken from edge-plasma simulations of Sec. 5.2. The ion flux on the divertor target is given by

$$\Gamma_d = n C_s \frac{B_\theta}{B} \sin \alpha , \tag{5.3-6}$$

where the last two terms account for the inclination of the target plate with respect to the field line. In estimating the divertor erosion rates, the ion flux is calculated at different target locations to account for the variable flux and energy of incident ions. The flux to the first wall is assumed to be purely diffusive and is estimated from

$$\Gamma_{fw} = -D_a \nabla n \approx \frac{D_a n_{fw}}{\lambda_{fw}} , \tag{5.3-7}$$

where λ_{fw} is the radial density e-folding length at the first wall.

5.3.1. First-Wall Erosion

The first-wall erosion is assumed to be limited by the erosion of carbon from the silicon-carbide (SiC) matrix, with an effective specific gravity of the carbon inside the SiC of 1.5. No credit is given for redeposition at the first wall since the ionized impurities will be swept along the field lines to the target away from the sputtered source region. The ion flux to the first wall is estimated at 10^{19} $m^{-2}s^{-1}$ and the helium flux is assumed to be in proportion to the helium density fraction. The plasma temperature at the first wall is estimated to be ~20 eV. To be conservative, it is assumed that a sheath will form at the first wall which will accelerate the ions. The result of this assumption is that ion

energies will strike the wall in the range of 80 (D,T) to 140 eV (He), where the sputtering yield for carbon is near its maximum value.

The estimated erosion rates of the ARIES-I first wall are given in Table 5.3-I. These estimates do not include erosion caused by charge-exchange neutrals, which was considered in "The TITAN Reversed-Field-Pinch Reactor Study" [8]. During that study, a multi-group neutral-diffusion code was used to calculate the flux and energy of charge-exchanged neutrals. It was seen that the neutrals that charge exchanged at hotter plasma locations contributed to the erosion rate. However, for ion temperatures above the 10 to 20 eV range, the charge-exchange neutral contribution was small.

Since there is some uncertainty in the estimated value of the plasma temperature at the first wall, the erosion rates due to tritium ions are calculated using similar flux conditions but for different values of the first-wall ion temperature. The results are given in Table 5.3-II.

Table 5.3-I.
Estimated Erosion Rate of the ARIES-I First Wall[a]

Ion Species	Erosion Rate (mm/y)
Tritium	0.12
Deuterium	0.08
Helium	0.06
TOTAL	0.26

[a]For temperature of 20 eV, no redeposition, and assuming sheath formation which accelerates the ions.

Table 5.3-II.
Sensitivity of the Erosion Rate of the First-Wall by Tritium[a]

Plasma Temperature (eV)	Erosion Rate (mm/y)
50	0.24
25	0.15
20	0.12
10	0.03
5	0.01

[a]Using the same flux conditions as in Table 5.3-I.

5.3.2. Divertor-Target Erosion

Significant redeposition is expected at the target plate, as opposed to the first wall. For the ARIES-I plasma conditions, the net erosion of tungsten is estimated to be 0.03 to 0.15 of the gross erosion (redeposition rates of 0.97 to 0.85, respectively); the exact value depends on plasma temperature and divertor target geometry. To be conservative, therefore, a redeposition rate of 0.85 was used for the ARIES-I estimates.

For an estimated divertor target temperature of 25 eV, the erosion of tungsten by D or T is found to be negligible and the erosion rate is dominated by helium ions. Self-sputtering is found to result in a <3% increase over the plasma-ion sputtering for temperatures even as high as 50 eV. The total erosion rate of the divertor target plate is estimated at 0.5 mm/y.

The sensitivity of the divertor-target erosion rate to the plasma temperature, using similar flux conditions, is shown in Table 5.3-III. As expected, above 30 to 40 eV, the erosion rate becomes significantly larger. Erosion of the divertor plate due to plasma disruptions is discussed in Sec. 5.5.

Table 5.3-III.
Sensitivity of the Erosion Rate of the Divertor by Helium[a]

Plasma Temperature (eV)	Erosion Rate (mm/y)
50	3.0
40	2.5
30	0.8
25[b]	0.5
20	0.01

[a]For the same flux conditions (erosion rate is dominated by He).

[b]Estimated temperature at the ARIES-I divertor.

5.4. DIVERTOR DESIGN AND ENGINEERING

5.4.1. Divertor Material and Manufacturing

The ARIES-I reactor uses high-recycling divertors to reduce the plasma ion temperature at the divertor plate to below the sputtering threshold for high-Z materials, and it achieves very low erosion of the divertor target [9]. Molybdenum, tungsten, and several tungsten-tantalum-rhenium alloys were considered for the ARIES-I divertor-target material. All have similar favorable thermomechanical characteristics. Since all of these materials activate in a fusion-neutron environment, their use was limited to providing the armor for the ARIES-I divertor. For a thin, plasma-sprayed coating on a structural substrate, alloying elements were not thought to be needed. The neutron activation properties of molybdenum, tantalum, and rhenium lead to long-lived products that would cause waste disposal concerns. Tungsten is the least activating of the high-Z materials [10] and is chosen for ARIES-I. To minimize the accident dose potential and waste disposal problems of tungsten, isotopic tailoring is also specified (Sec. 10).

Helium is chosen as the coolant to ensure compatability with the blanket cooling system. Vanadium cooling tubes were initially considered for the divertor structure.

However, concern about differential thermal expansion between the tungsten and the vanadium, and about tritium diffusion into the divertor coolant led to an investigation of SiC composites. Tritium ions from the plasma will implant into the tungsten target. To minimize diffusion of this implanted tritium through the tungsten into the helium coolant, a low permeability substrate (*e.g.*, SiC) should be used. The thermal expansion coefficient of SiC and tungsten are very similar, which reduces concerns about the thin surface layer spalling off the substrate. The high-temperature capability of SiC allows the ARIES-I divertor to handle the high heat fluxes ($\sim$5 MW/m^2) with coolant inlet/outlet temperature conditions the same as those used for the blanket. This in turn allows efficient recovery of the divertor power.

Construction of the ARIES-I divertor target begins with a bank of SiC composite tubes. The tubes are formed by helically winding SiC fiber around a tapered mandrel. After winding, the fibers are infiltrated to form the SiC matrix and the mandrel is removed leaving behind the composite tube. (Additional details on the process of composite manufacture are discussed in Sec. 8.) The tubes have a nominal outside diameter of 2.5 mm and a wall thickness of 0.5 mm. The tube diameter varies along the length to form the necessary pie shape when the tubes are placed side-by-side.

The plasma-facing side of the tube bank has a plasma-sprayed tungsten coating. The back of the SiC-composite tube bank is coated with a high density layer of chemical-vapor-deposited (CVD) SiC, which adds strength to the structure and ensures leak tightness of the tubes. The targets are then fitted into the supply and collection headers and brazed into place. Two upper and two lower targets are installed into each of the 16 fusion-power-core modules. A completed target assembly is shown in Fig. 5.4-1.

5.4.2. Divertor Configuration

The basic configuration of the divertor target is illustrated in Fig. 5.4-1. The coolant flows in the poloidal direction. The coolant supply headers are located under the private-flux region and the coolant inlet is at the outboard strike point. The coolant collection headers are at the ends of the inboard and outboard target sections. This arrangement allows the target area with the maximum heat-flux to be cooled by the lowest temperature coolant. The peak heat flux on the divertor plate is estimated at 4.5 MW/m^2 (Sec. 5.2). Because of large uncertainty in edge-plasma parameters and because the heat-flux estimate given above does not account for such factors as toroidal asymmetries or target misalignment, an engineering safety margin of $\sim$2 was chosen as the divertor design goal (*i.e.*, localized heat fluxes twice as large as the estimated value can be handled).

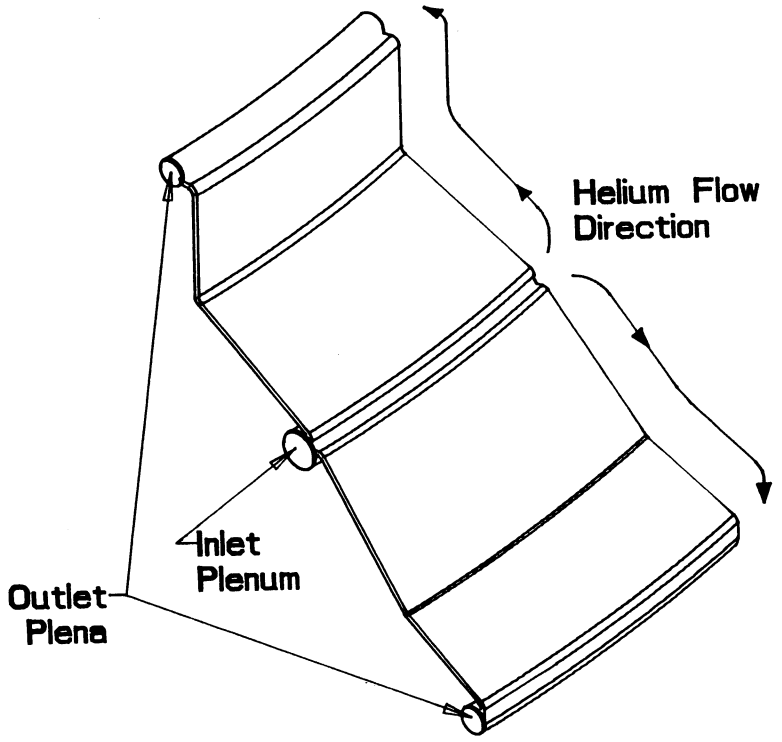

Figure 5.4-1. Isometric view of one of the ARIES-I divertor targets.

The thermal-hydraulic design of the divertor constrains the divertor plate configuration (inclination angle with respect to the field lines). The minimum-size divertor-target area can be achieved by contouring the target surface in such a way that the heat flux is constant on the target (by increasing the inclination angle away from the strike point). The thermal-hydraulic analysis of such a plate for ARIES-I, however, showed that the design has a heat-flux safety margin on the order of 1.

To achieve a larger safety factor (on the order of 2), the target surface is contoured to have an inclination angle of 10° with respect to field lines in the poloidal plane for 0.60 m away from the strike point. In this region, the heat flux is reduced (exponentially) to $\sim$1 MW/m^2. The remaining 0.40 m of the target is contoured to have a constant heat flux of 1 MW/m^2. By contouring the target in the low flux region, the size of the target can be reduced and thereby provide more clearance behind the target for shielding. Divertor coolant tubes have a hydraulic diameter of 2.5 mm and a wall thickness of 0.5 mm.

The heat-flux profile on the ARIES-I outboard divertor target is shown in Fig. 5.4-2. The coolant temperature rise along the flow path is also plotted. The coolant inlet and exit temperatures are, respectively, 350 and 650 °C and the coolant pressure is 10 Mpa, the same as those of the blanket coolant circuit. As a result, the divertor coolant circuit is connected to the main heat-transport system and the divertor power is recovered by

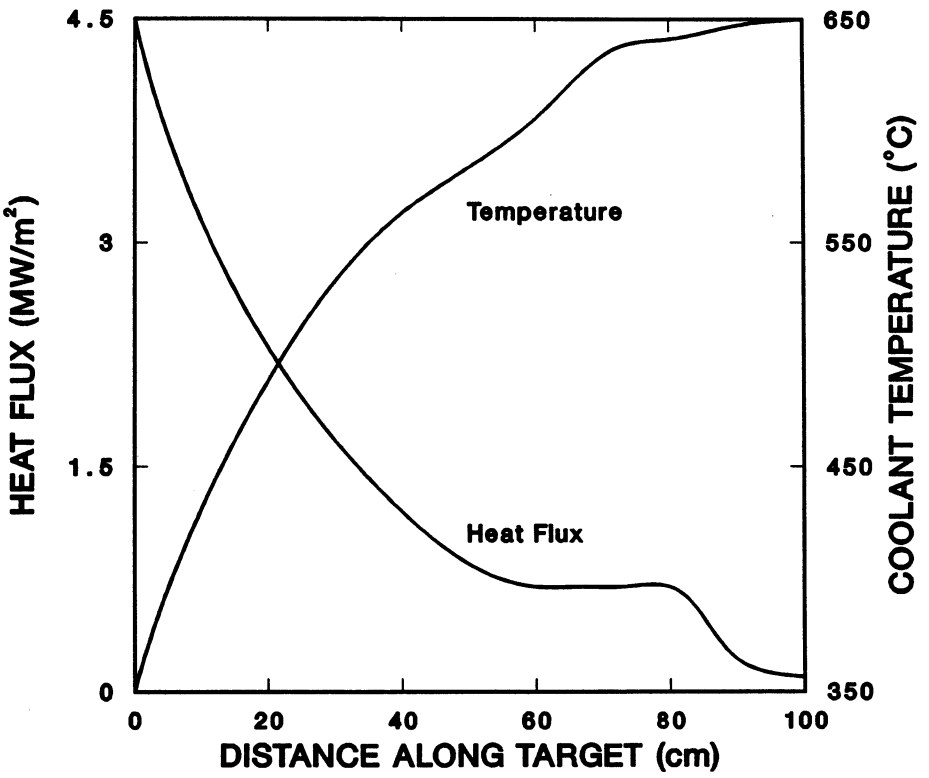

Figure 5.4-2. Heat flux and coolant temperature profiles along the ARIES-I outboard divertor target.

the main thermal-conversion cycle at a gross efficiency of 49%. The divertor coolant, however, must flow at about 150 m/s to remove the high heat flux without exceeding the temperature limit of the interface between the SiC and the tungsten coating. This flow rate causes a substantial drop in pressure and increases the pumping power requirement. The required circulator power for the divertor cooling circuit is 35 MWe, which represents 12% of the recovered thermal power from the divertor coolant circuit. Although the required pumping power is relatively large, the benefits of using helium as the coolant seem to outweigh the drawbacks.

5.4.3. Finite-Element Thermostructural Analyses

Thermostructural analyses of the ARIES-I divertor target were performed using the ANSYS finite-element code [11]. The material properties used in the analyses are listed in Table 5.4-I. The critical location for the divertor is at the coolant inlet, where the maximum surface heat flux of 4.5 MW/m^2 occurs. Therefore, a 2-D model of the a single

coolant tube in the divertor plate, at the coolant inlet location, was constructed using PATRAN [12] (symmetry between neighboring tubes is assumed). Figure 5.4-3(A) shows the model which comprises 348 quadrilateral elements. The large number of elements was necessary to properly analyze the interface between the SiC composite tube and the tungsten coating.

Table 5.4-I.
Material Properties Used in Thermostructural Analyses of the ARIES-I Divertor[a]

	SiC Composite	Tungsten
Density (kg/m^3)	3,000	19,000
Young's modulus (GPa)		
E_x	364	370
E_y	360	370
Poisson's ratio, ν	0.16	0.20
Thermal-expansion coefficient (10^{-6}/K)		
α_x	4.4	4.5
α_y	4.3	4.5
Thermal conductivity (W/K-m)		
k_x	15	113
k_y	12	113
Allowable stress (MPa)	190	200
Maximum temperature (°C)	1,100	1,200[b]

[a]The x and y directions are, respectively, along and perpendicular to the plate (see Fig. 5.4-3).

[b]Temperature limit at SiC-composite/W interface.

5.4.3.1. Thermal analysis

Figure 5.4-3(B) gives the temperature contours in the divertor plate at the coolant inlet location for a surface heat flux of 4.5 MW/m^2 (estimated peak heat flux on the ARIES-I divertor plate). The coolant bulk temperature at this point is 350 °C. A heat transfer coefficient of 12.9 $kW/K\text{-}m^2$ is used and all other surfaces are assumed to be adiabatic. A volumetric heating rate of 23 MW/m^3 is also applied to all of the elements in the model.

Figure 5.4-3(B) shows that the temperature distribution in the tungsten layer facing the plasma is approximately 1-D with significant conduction to the location between touching tubes. The lower thermal conductivity of SiC relative to tungsten is clearly reflected by the larger temperature gradient inside the SiC-composite coolant wall. The peak temperatures are 776 °C in the tungsten layer and ~692 °C at the SiC-composite/W interface. All materials operate below their respective temperature limits (Table 5.4-I).

5.4.3.2. Stress analysis

Generally, when two dissimilar materials are in contact and exposed to a heat load, the difference in thermal expansion coefficients of the materials causes differential expansion of the two materials. Therefore, high stress concentrations can exist at the termination of the interface at the free surface of the component. However, the material choice for the ARIES-I divertor plate minimizes the stress concentrations in the interface because SiC and tungsten have nearly identical thermal-expansion coefficients. Furthermore, because of the ability of tungsten to undergo plastic deformation, the stress concentrations predicted by the finite-element analysis are assumed to be adequate in assessing the viability of the ARIES-I divertor-plate design.

Because relevant uniaxial stress measurements are not yet available for ceramic-matrix composite materials, the von Mises stress is used to indicate the equivalent thermal-stress levels [shown in Fig. 5.4-4(A)]. The peak thermal stresses are ~86 MPa in SiC and ~66 MPa in tungsten. These stresses fall well below the maximum-allowable stress limits of, respectively, 190 and 200 MPa. Furthermore, the location of these stress concentrations is between neighboring tubes, which is not the most critical location in the divertor. The combined thermal-plus-pressure stress contours induced by the 10-MPa coolant are shown in Fig. 5.4-4(B). This combined stress is 121 MPa, which is also well below the allowable stress limit of 190 MPa.

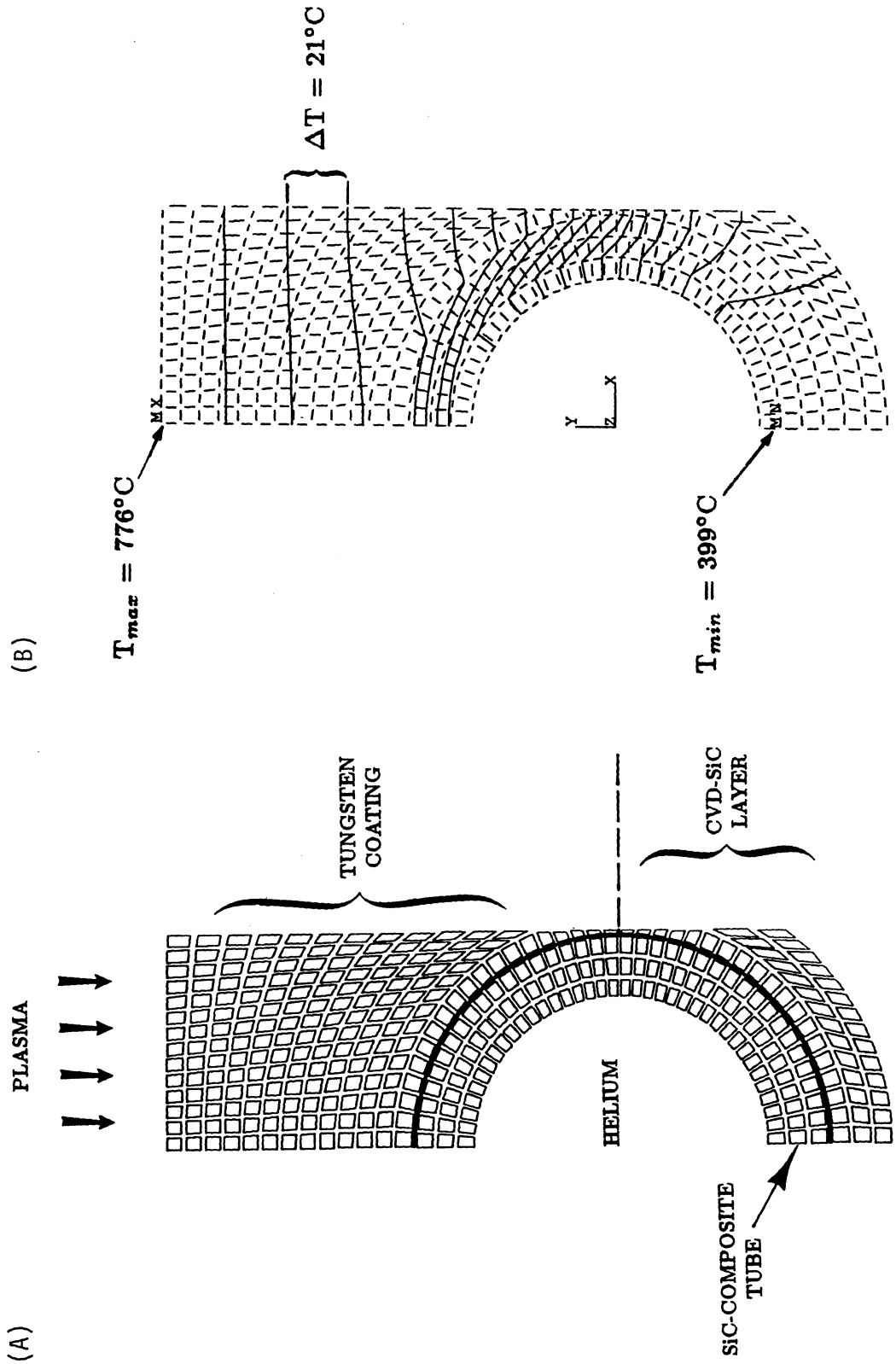

Figure 5.4-3. The finite-element thermostructural analysis of the ARIES-I divertor plate: (A) model and (B) temperature contours for a surface heat flux of 4.5 MW/m^2. (A 2-mm-thick CVD tungsten layer faces the plasma.)

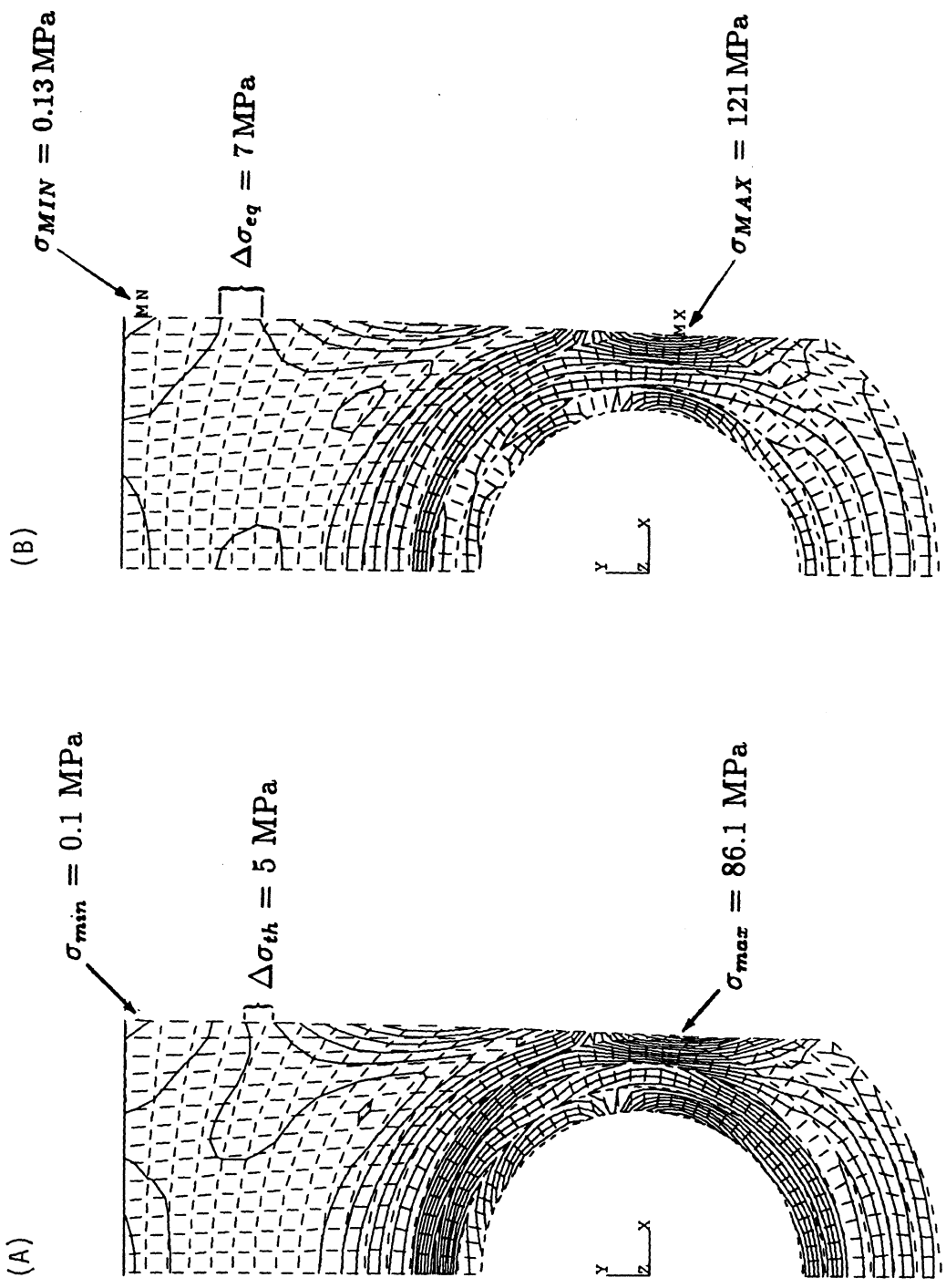

Figure 5.4-4. Contours of (A) equivalent thermal-stress and (B) combined thermal-plus-pressure stress in the ARIES-I divertor for a surface heat flux of 4.5 MW/m^2 and coolant pressure of 10 MPa.

5.4.3.3. Engineering safety factor

One of the important issues regarding plasma-facing components is the requirement for the component to withstand load excursions, asymmetries, and peaking due to misalignment. Using the finite-element model outlined above, it was found that at a steady-state surface heat load of 8 MW/m^2, the maximum stress concentration inside the SiC composite material does not exceed the 190-MPa limit. The maximum temperature is also below the allowable value of 1100 °C for the SiC/W interface. For this heat flux, the contours of the temperature and the combined thermal-plus-pressure stress are shown in Fig. 5.4-5. For a peak heat flux of 9 MW/m^2, the SiC/W interface temperature is calculated at 1043 °C and the peak equivalent stress in SiC is 190 MPa (allowable values are, respectively 1100 °C and 190 MPa). Therefore, the divertor has an engineering design margin of 2.

5.5. THERMAL RESPONSE TO PLASMA DISRUPTION

The divertor plate of ARIES-I is made of a bank of silicon-carbide (SiC) composite coolant tubes which are coated with a 2-mm layer of tungsten on the plasma-facing side. Providing that the divertor target plate remains intact following a full-power disruption (as is expected to be the case), the thermal ablation of the tungsten coating determines the number of disruptions after which the divertor plate should be recoated (or replaced).

Approximate, 1-D, transient heat conduction with phase change and moving vapor/liquid and liquid/solid boundaries has been used to predict the thermal erosion of a plasma-facing component due to plasma disruptions [13 – 15]. Other phenomena might also affect the thermal erosion (*e.g.*, possible reduction of the incident heat flux due to the formation of a vapor shield, movement and stability of the melt layer under electromagnetic and other forces, redeposition of the vaporized materials, thermo-fluid dynamics of the melt layer, *etc.*). Approximate analyses of vapor shielding have been done [16 – 18], but the results vary considerably. For ARIES-I disruption analyses, the thermal response of the divertor plates has been analyzed with a transient 2-D code. The thermo-fluid dynamic behavior of the melt layer is also studied using a transient 2-D code; a simple vapor-shield model was included. This section describes the results of this analysis.

Since the physics of disruptions is uncertain, the plasma disruption parameters for ARIES-I (Table 5.5-I) are chosen to correspond to, or to fall within the range of, those

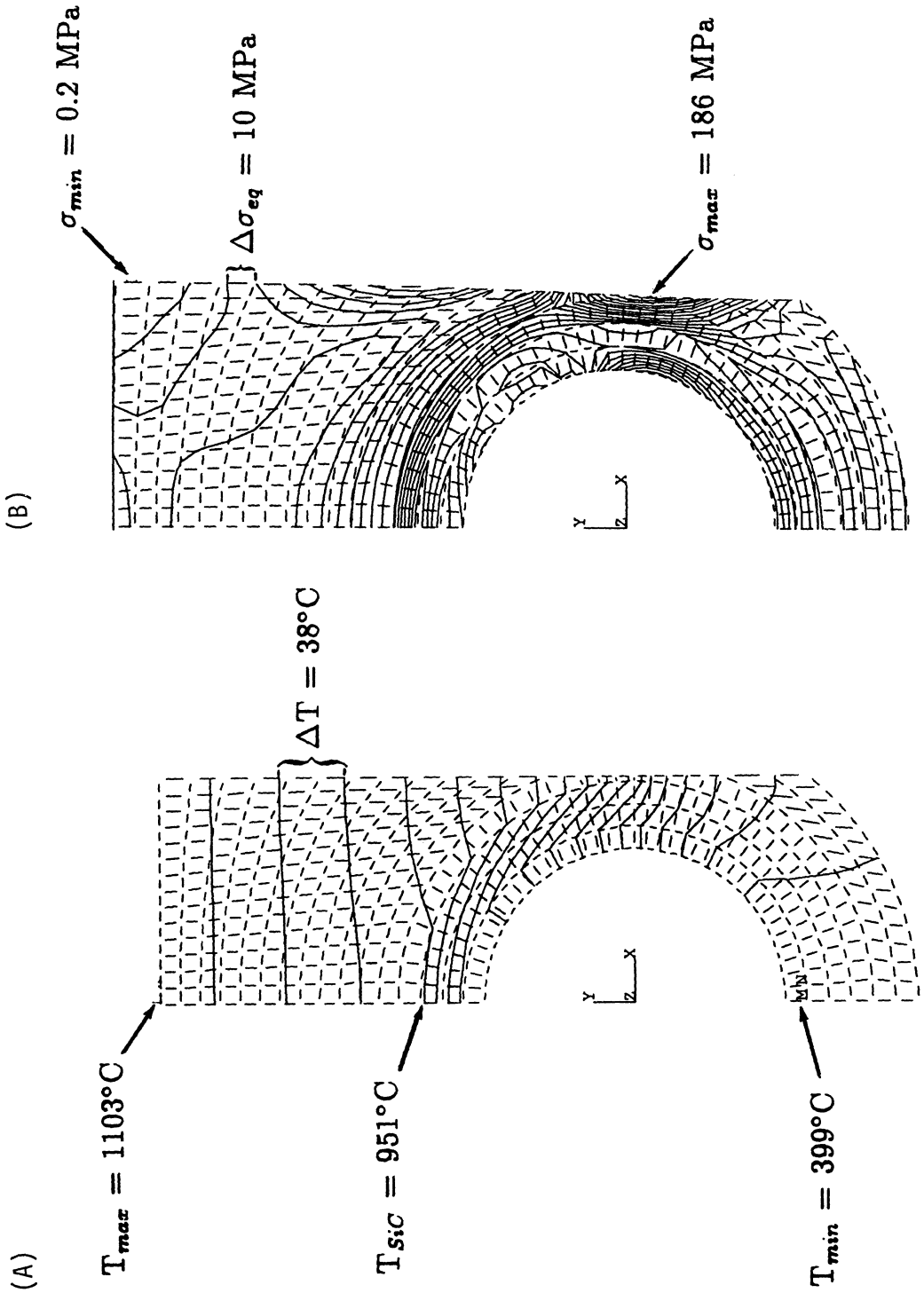

Figure 5.4-5. Contours of (A) temperature and (B) combined thermal-plus-pressure stress in the ARIES-I divertor for a surface heat flux of 8 MW/m^2 and coolant pressure of 10 MPa.

Table 5.5-I.
Parameters Used in Ablation Calculations

Thermal quench time (ms)	0.3
Energy deposited on divertor plate (MW)	375
Total divertor plate area (m^2)	142
Local peaking factor for heat flux	5
Divertor plate heat flux (GW/m^2)	
Average	8.8
Peak	44.
Initial temperature of W (°C)	1,100
Thickness of W coating (mm)	2

predicted for ITER [19]. To be conservative, it is assumed that: (1) all disruptions occur at full plasma power; (2) one half of the total thermal energy in the plasma is deposited on one of the divertor plates; (3) during subsequent disruptions, the disruption energy appears on the same divertor plate and the local peaking factor of 5 remains constant at the same location; (4) the evaporated tungsten is not redeposited on the divertor plate; (5) the properties of tungsten are assumed constant; (6) only 1 mm of the tungsten coating is for disruption protection (the other 1 mm is for sputtering erosion); and (7) the initial temperature of tungsten is 1100 °C everywhere on the divertor plate, well above the estimated peak tungsten temperature of 776 °C (Fig. 5.4-3).

An upper bound for the maximum local ablation of tungsten can be found through an adiabatic calculation in which it is assumed that only the tungsten that evaporates absorbs the energy. The absorbed energy raises the temperature from the initial temperature to the melting point, changes the phase from solid to liquid, raises the liquid temperature to the boiling point, and then evaporates the material. The remaining tungsten stays at the initial temperature. Such a calculation is conservative since it neglects conduction into the metal. For ARIES-I, an adiabatic calculation gives a maximum local ablation of 130 μm per disruption (for an initial tungsten temperature of 1100 °C). Therefore, the 2-mm tungsten coating would withstand, at least, about 14 full-power disruptions.

5.5.1. Model

Thermal response of the ARIES-I divertor plate to plasma disruption and the fluid dynamics of the melt layer have been analyzed numerically using 2-D codes. The ARIES-I divertor plate is modeled as a composite flat plate of 2-mm-thick tungsten over 0.5-mm of SiC. Plasma particle and heat fluxes are incident on the tungsten coating. The model is shown in Fig. 5.5-1 with the x direction pointing into the plate and y being along the plate. The peak and average heat fluxes are denoted by q_1'' and q_2'', respectively. Because of this lateral variation of the heat flux, the problem should be solved in two dimensions.

5.5.1.1. Thermal response models

The thermal response of the divertor plate is estimated by a 2-D code [20]. This code solves the transient energy equation for temperature, $T(x,y;t)$:

$$\frac{\partial(\rho c_p T)}{\partial t} = \frac{\partial^2(kT)}{\partial x^2} + \frac{\partial^2(kT)}{\partial y^2} + Q\,, \qquad (5.5\text{-}1)$$

where t is time, and ρ, c_p, and k are, respectively, the density, specific heat, and thermal conductivity of the plate material. The volumetric heat source, Q, is assumed zero for this problem.

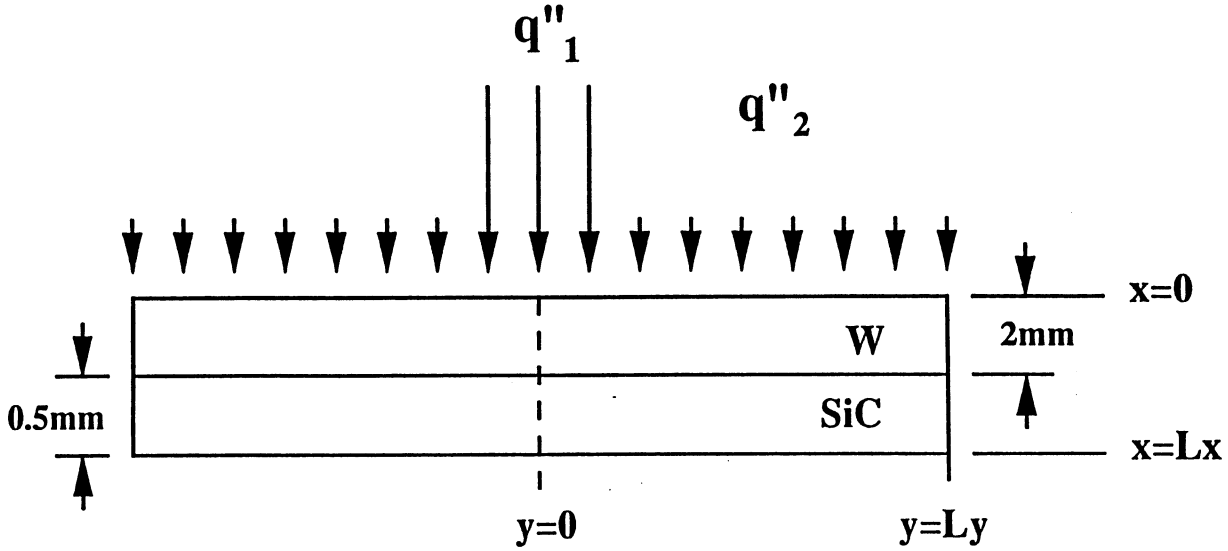

Figure 5.5-1. Model of the divertor plate for thermal and fluid dynamic analysis of a plasma disruption.

The boundary conditions, in addition to symmetry conditions at $y = 0$ and $y = L_y$ surfaces (see Fig. 5.5-1), are

$$\begin{aligned} -\left.\frac{\partial T}{\partial x}\right|_{x=0} &= q''_{pl}(t,y) \\ -\left.\frac{\partial T}{\partial x}\right|_{x=L_x} &= h(T_{x=L_x} - T_{cool}) , \end{aligned} \tag{5.5-2}$$

where T_{cool} is the coolant temperature and h and $T_{x=L_x}$ are, respectively, the heat transfer coefficient and temperature at the $x = L_x$ surface. The heat flux, $q''_{pl}(t,y)$, at $x = 0$ accounts for the incident heat flux, including vapor shielding, on the plate.

The vapor/liquid and liquid/solid surfaces are treated as moving fronts and appropriate conditions are applied. The code uses the evaporation model of Ref. [17] which is based on the numerical model of Ref. [21]. The simple vapor-shield model of Ref. [16] is also used, in which the heat flux reaching the plate surface, $q_{pl}(t,y)$, is given by

$$q''_{pl}(t,y) = \begin{cases} q''_R \left(1 - \dfrac{\Delta x(t)}{2\chi}\right), & \text{for } \Delta x(t) < \chi \\ \dfrac{q''_R}{2}, & \text{for } \Delta x(t) \geq \chi \end{cases} . \tag{5.5-3}$$

In this equation, q''_R, is the plasma heat flux to the plate, χ is the range of the plasma ions into the plate materials, and $\Delta x(t)$ is the plate thickness vaporized by time t from the initiation of the thermal quench. This model assumes that once χ depth of the plate material has been evaporated, all the incident energy is absorbed by the vapor shield and then instantly reradiated, 50% going to the plate and the other 50% going away from the plate.

5.5.1.2. Thermo-fluid dynamic-response models

A 2-D code [22] is used to analyze the thermo-fluid dynamic behavior of the melt layer. This code is based on the numerical solution of the transient energy equation (convection-diffusion equation) and the Navier-Stokes equation in the Boussinesq approximation for the temperature and velocity fields, respectively:

$$\frac{\partial T}{\partial t} + \mathbf{u}\cdot\nabla T = \nabla\cdot(k\nabla T) + Q , \tag{5.5-4}$$

$$\frac{\partial \mathbf{u}}{\partial t} + (\mathbf{u}\cdot\nabla)\mathbf{u} = -\frac{1}{\rho}\nabla p + \nu\,\nabla^2\mathbf{u} - \beta\,\mathbf{g}\,\Delta T , \tag{5.5-5}$$

where p is the pressure, $\mathbf{u}(u,v,w)$ is the velocity, ν is the kinematic viscosity, β is the thermal coefficient of expansion, and g is the gravitational acceleration. The volumetric heat source in the melt layer is assumed zero for this problem. Instead of the continuity equation, the code solves the Poisson equation for pressure.

$$\nabla^2 p = -\frac{\partial D}{\partial t} + \nu \nabla^2 D - \nabla \cdot [(\mathbf{u} \cdot \nabla)\mathbf{u}], \tag{5.5-6}$$

where $D = \nabla \cdot \mathbf{u}$.

The Neumann boundary condition for temperature and a no-slip condition for velocity are applied at the liquid/solid interface. At the liquid/vapor surface, the stress condition

$$\mu \frac{\partial u}{\partial x} = -S \frac{\partial T}{\partial y} \tag{5.5-7}$$

is applied, where μ is viscosity and S is the temperature coefficient of surface tension. The surface at $x = L_x$ is assumed adiabatic since heat transfer at this surface is negligible. At the plasma-facing surface, the heat flux condition that accounts for radiation and evaporation is applied. The evaporation rate is estimated by an equation for a specific evaporation rate for idealized evaporation ($\alpha = 1$) for elements in high vacuum [23]:

$$m_{evap} = 4.4 \times 10^{-2} \alpha p_s \left(\frac{M}{T_v}\right)^{1/2}; \tag{5.5-8}$$

m_{evap} is specific evaporation rate, α is the evaporation coefficient, M is the molecular weight of the evaporant, T_v is the evaporant temperature, and p_s is the corresponding saturation pressure. This code does not account for vapor shielding. As is shown in the next section, vapor shielding has little effect on the melt layer thickness.

5.5.2. Results and Discussion

The model of the vapor shield is very simple at present. Therefore, the thermal analysis is performed with and without the vapor shield. Figure 5.5-2 shows the maximum plate temperature as a function of time. The maximum temperature of about 8000 °C is reached in a very short time (~0.01 ms) and drops rapidly at the end of the thermal quench time. With vapor shielding, the maximum temperature is reduced by about 600 °C.

Figure 5.5-3(A) shows the variation of surface temperature along the plate at the end of the thermal quench time (0.3 ms). The surface temperatures in the regions of peak

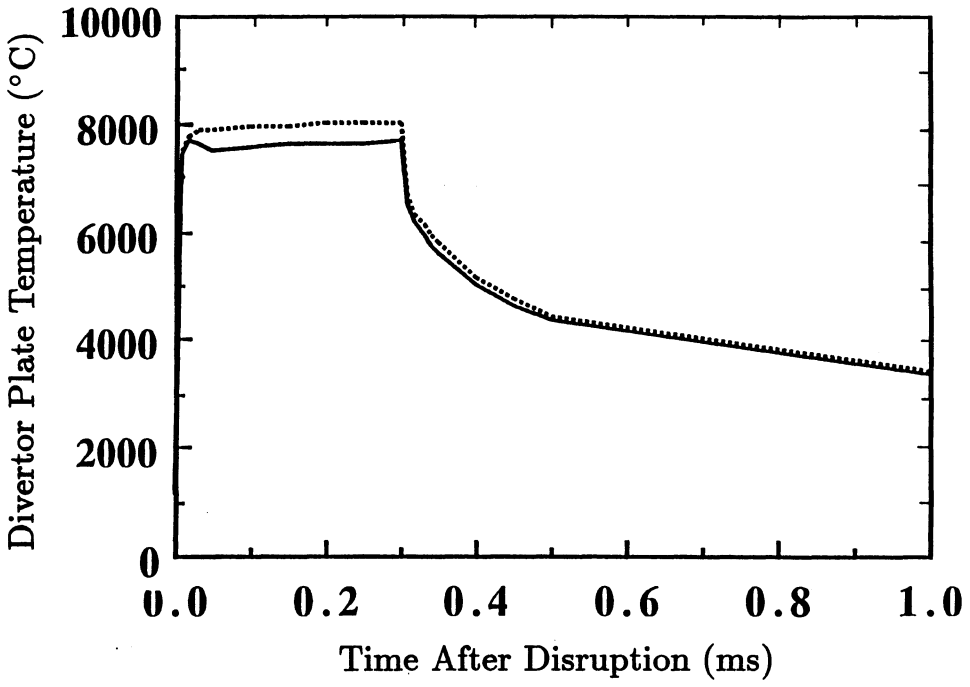

Figure 5.5-2. Time variation of the divertor-plate maximum temperature with (solid lines) and without vapor shield (dotted line).

and average heat fluxes are uniform, and the temperature gradient between these two regions is very steep. Although the heat fluxes in these two regions differ by a factor of 5, the temperature difference is only about 1000 °C. This is most likely caused by the large heat of vaporization and thermal conductivity of the tungsten. Vapor shielding reduces the temperatures in the peak and average heat-flux regions by about 350 and 250 °C, respectively.

The center temperature in the peak heat-flux region at the end of the thermal quench time (0.3 ms) is shown in Fig. 5.5-3(B) as a function of x (distance into the plate). The slope of the temperature profile is very steep, which might cause large thermal stress so a stress analysis needs to be performed. By the end of the thermal quench time, the temperature rise has penetrated only ~0.36 mm into the 2-mm-thick tungsten coating. The reduction of the material temperature due to the vapor shield is small.

Total evaporation of the tungsten coating is shown in Fig. 5.5-4(A) as a function of time after the disruption. The cumulative evaporation rate is nearly linear with and without the vapor shield. In both cases, evaporation stops quickly after the end of the thermal quench time when the surface temperature drops rapidly (Fig. 5.5-2). The total

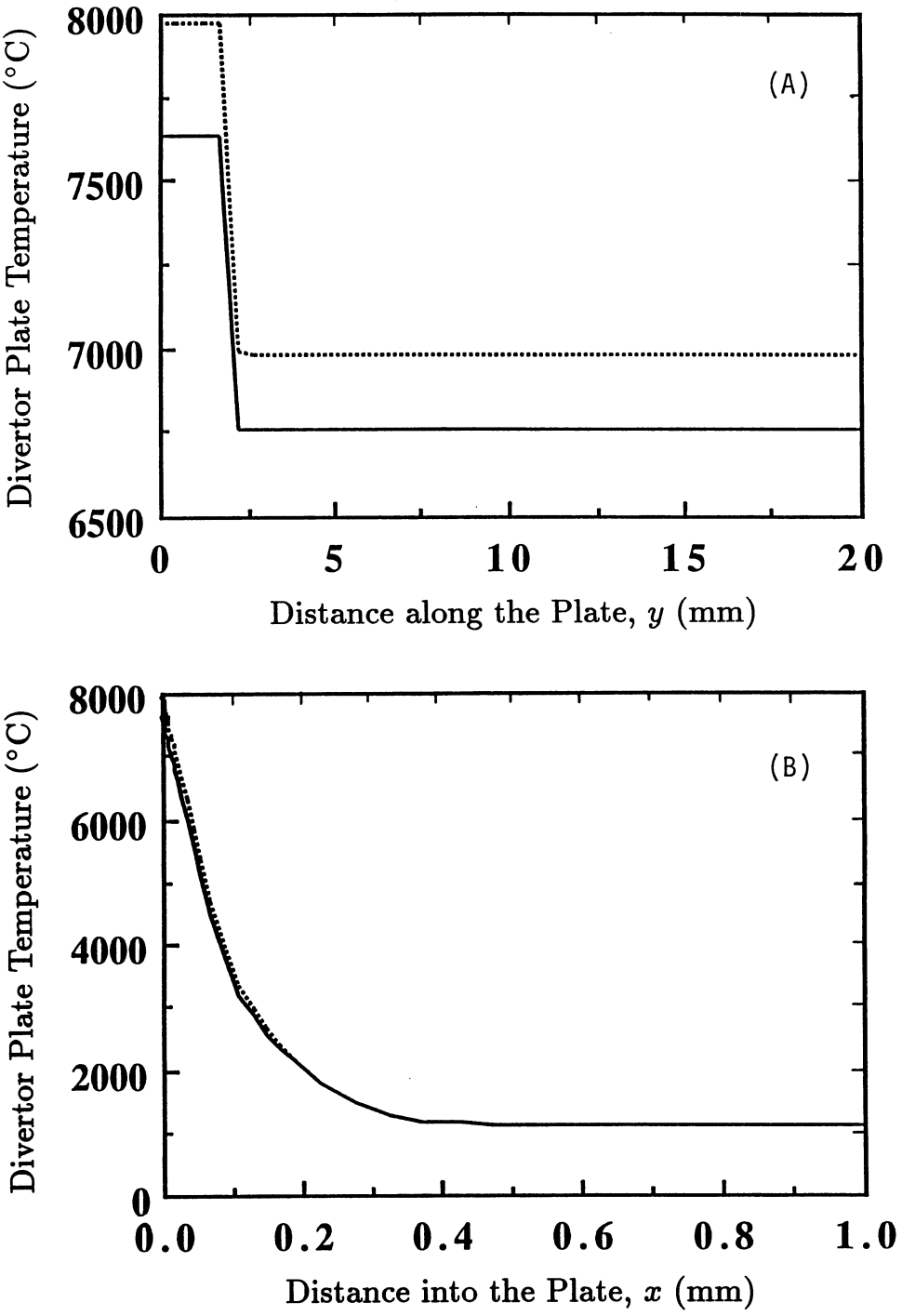

Figure 5.5-3. The divertor plate temperature at the end of thermal quench time (0.3 ms): (A) surface ($x = 0$) temperature along the plate and (B) temperature distribution into the plate at the location of the center of the peak heat flux region ($y = 0$).

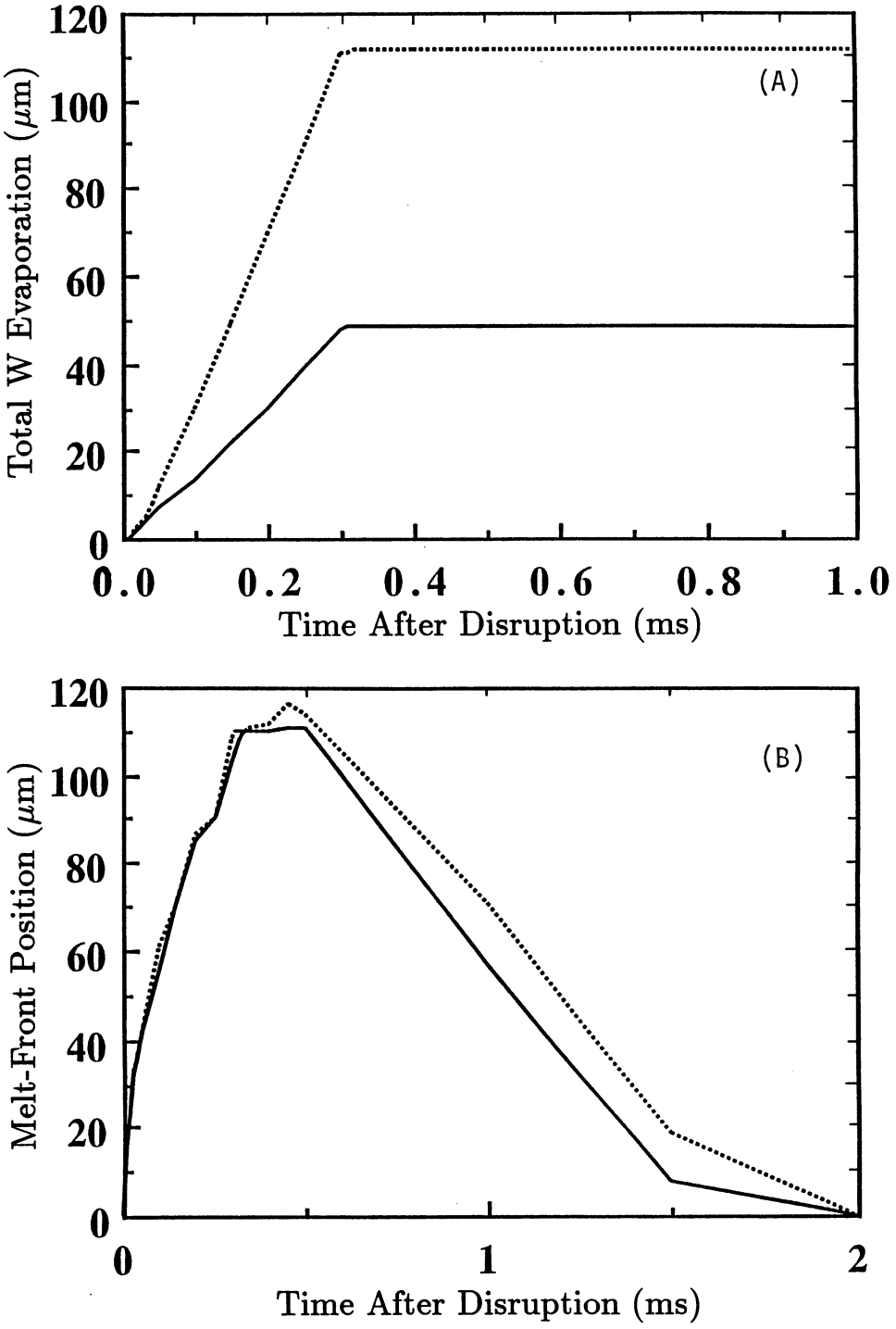

Figure 5.5-4. The response of the ARIES-I divertor plate as a function of time after disruption: (A) total evaporation thickness of tungsten coating (in μm) and (B) position of the melt front from the plasma-facing surface.

W evaporation rates with and without the vapor shield are, respectively, about 48 and 110 μm. One half (1 mm) of the tungsten coating designated for disruption protection may, therefore, last about 20 plasma disruptions, or about 10 disruptions without vapor shielding effects. However, the present vapor-shield model is very simple and further work is necessary to develop one that is more realistic. In addition, the contribution from the neglected effects, such as melt layer motion and stability, may be significant.

The time variation of the distance of the melt front from the top surface of the plate is shown in Fig. 5.5-4(B). The maximum melt-layer thickness is about 113 μm. The melt layer advances even after the end of the thermal quench time (0.3 ms) because of the conduction of the sensible heat of the melt layer into the solid. Resolidification starts at about 0.5 ms, and the time to the end of resolidification is more than 5 times the thermal quench time. Vapor shielding reduces the melt layer thickness only slightly.

Figure 5.5-5 shows the temperature contour, liquid velocity, and stream lines in the melt layer at the end of the thermal quench time. The driving forces for the liquid motion are the surface tension and buoyancy forces. This analysis does not account for vapor shielding. But, as shown in Fig. 5.5-4(B), the melt layer thickness is only very slightly affected by the vapor shield. The liquid motion appears to be very small and is confined to the junction area between the peak and the average heat-flux regions. The effect of this liquid motion on convective heat transfer may not be significant under the assumed conditions. A more rigorous analysis of the thermo-fluid dynamic behavior of the melt layer must account for the electromagnetic and recoil forces which are probably crucial for the melt layer motion. Further work is necessary to address these effects.

5.6. PELLET FUELING SYSTEM

High speed injection of frozen macroscopic (mm size) pellets of hydrogen isotopes has become the leading technology for fueling magnetically confined plasmas for controlled-thermonuclear fusion research. This approach has been demonstrated conclusively on a number of toroidal magnetic-confinement configurations including tokamaks, stellarators, and reversed-field pinches. Other related effects such as beneficial improvements in energy confinement properties, which have also been observed experimentally on several confinement devices, are generally associated with modifications in the plasma density and/or temperature profiles as a result of the fueling or particle deposition profiles.

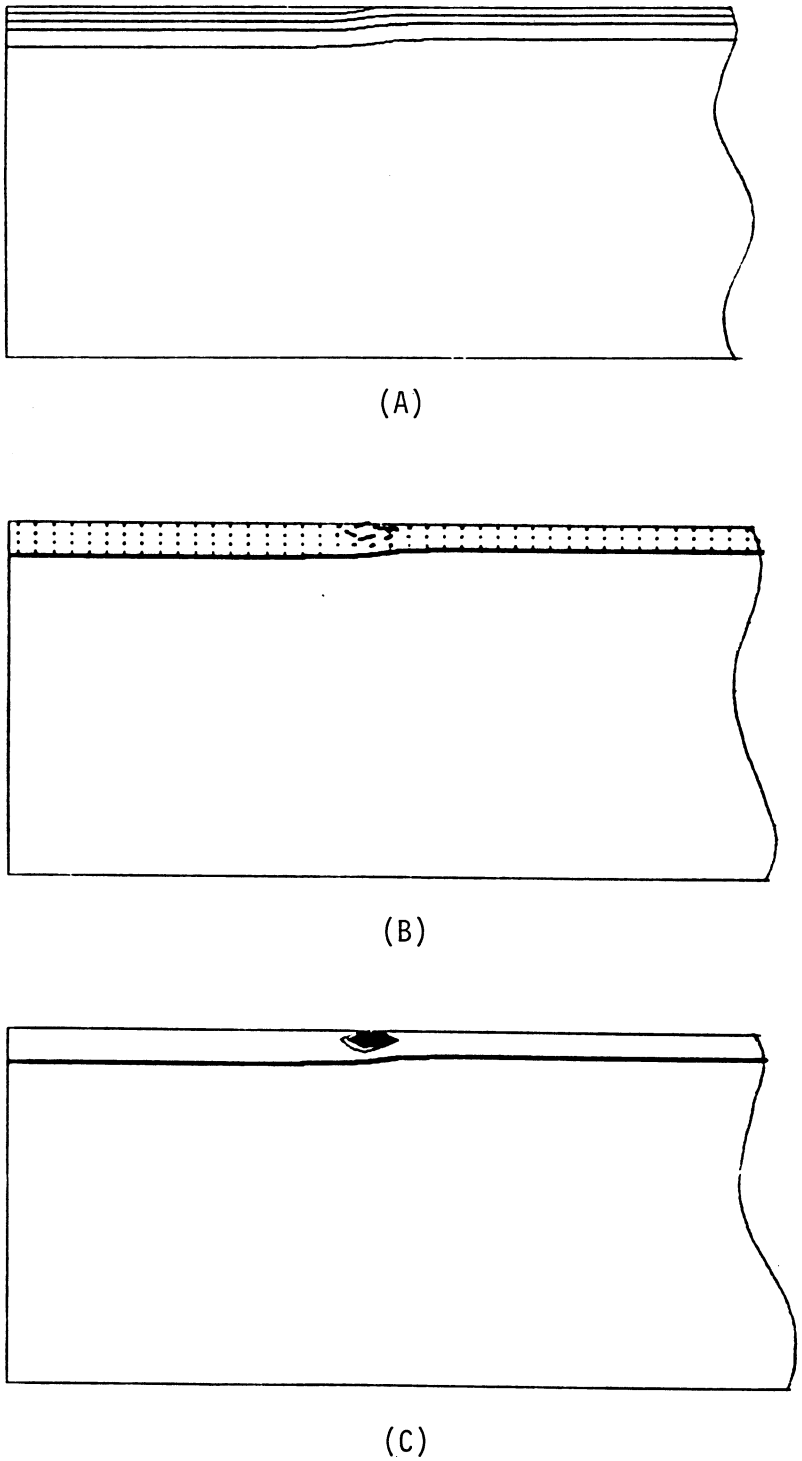

Figure 5.5-5. The melt layer characteristics at the end of the thermal quench time (0.3 ms): (A) temperature contour, (B) liquid velocity, and (C) stream lines.

5.6.1. Pellet-Injection-System Specifications

The pellet fueling requirements of present and future magnetic-confinement devices vary in accordance with the specific plasma parameters (the electron temperatures and densities which govern the pellet evaporation rate) and the physical and operating characteristics of the device (experiment pulse length, plasma volume, type of plasma limiter, *etc.*). With respect to pellet speed, it is desirable that the pellet have sufficient speed to penetrate a specified fraction of the distance to the magnetic axis. This requirement is linked to the evaporation rate of hydrogenic ice in a magnetized plasma. Although several theoretical models have been proposed to describe this process [25], the model that is most often found to be in agreement with the experimental measurements of pellet penetration is the so-called neutral-gas shielding model [26 – 29] (discussed in more detail in Sec. 5.6.1.1).

The ablation rate and, therefore, the penetration of the pellet strongly depends on the pellet size and the plasma electron temperature; the pellet size is normally constrained by the allowable density perturbation to the target plasma. The remaining fueling requirement is the injection frequency which is related to the rate at which the plasma must be replenished. This rate depends on the intrinsic plasma-particle replacement time and the net plasma-exhaust rate. The former is roughly proportional to the plasma volume and the latter is dependent on the plasma limiter configuration (material limiter, pump limiter, magnetic divertor). Small plasma devices with plasma volumes in the range of a few m^3 typically require pellet injection frequencies as high as 20 to 30 Hz to maintain the plasma density at steady-state levels. Larger devices, such as the Joint European Torus (JET), whose plasma volume exceeds 100 m^3 require injection frequencies in the 5-Hz range. Injection rates of a few Hz or lower will satisfy the requirements for ARIES-I (volume $\sim$500 m^3) and future fusion reactors.

All pellet injection concepts, whether simple or complex, share common technological problems associated with the unique properties of solid hydrogen. The isotopes of hydrogen (H_2, D_2, and T_2) freeze in the temperature range of 14 to 20 K [30] which necessitates the use of liquid-helium-cooled components for the production of solid material. High vacuum and low heat-loss techniques as well as the selection of suitable low-temperature, tritium-compatible, high-strength materials are important design considerations. The physical characteristics of hydrogen ice also play an important role, especially with respect to acceleration to the range needed for future reactor-grade plasmas. The densities of the solid hydrogen isotopes are low (200 and 300 kg/m^3, respectively, for D_2 and T_2), which is certainly an advantage in minimizing acceleration forces. For example, 6-mm deuterium pellets weighing only 35 mg can easily be accelerated to speeds in excess of

1 km/s in acceleration paths less than a meter long by single-stage light-gas-gun injectors operating at propellant gas pressures of 60 bar [31]. However, the yield strength of the solid is also small (~5 bar), which will probably place a rather low limit on tolerable acceleration forces. Two-stage light-gas guns subject deuterium pellets to accelerations of 5 to 9 $\times$ 10^6 m/s^2, corresponding to an equivalent acceleration pressure of 50 to 90 bars. Encasing the pellets in a capsule (known as a sabot) could further increase acceleration rates and eliminate pellet erosion at higher speeds [32].

5.6.1.1. Pellet ablation/penetration calculations

The neutral-gas shielding model [26-29] is generally in agreement with the experimental measurements of pellet penetration. According to this model, the surface of the pellet reacts to the intense plasma heat flux by expelling molecular hydrogen gas (which subsequently dissociates and ionizes) at a sufficiently high rate to partially shield the surface from the external plasma environment. The concept of the neutral gas shield is derived from the mechanism by which the plasma heat flux is attenuated by the gas cloud that envelopes the pellet. Heat transport to the pellet surface is accomplished via plasma electrons that penetrate the ablatant; in the early models, the electron flux was treated as a monoenergetic beam subjected to a continuous slowing-down process. In the ARIES-I formulation, the evaporation rate is governed by the stopping power of the ablation cloud. The effect is to increase the energy required to liberate a molecule from the surface of the pellet to about 2 eV, as compared to the sublimation energy of 0.01 eV. The rate at which the pellet surface recedes, given in terms of the local electron temperature, T_e, and plasma density, n_e, is

$$\frac{dr}{dt} = 3.1 \times 10^6 \frac{n_e^{1/3}\ T_e^{1.64}\ r^{-2/3}}{n_s^o}, \qquad (5.6\text{-}1)$$

where SI units are used except for T_e (which is in eV), $n_s^o = 3.1 \times 10^{28}$ m^{-3} is the molecular number density of the solid, and m is the molecular mass.

The time for complete evaporation of the pellet (the pellet lifetime) is determined by integrating Eq. (5.6-1) over the pellet trajectory. Of particular interest is the velocity required to penetrate to the magnetic axis of the plasma. For conditions in which the plasma temperature and density increase linearly with distance [*i.e.*, $T_e/T_e(0) = n_e/n_e(0) = 1 - x/a$, where x is the plasma radius and a is the minor radius, and (0) denotes the central conditions], the pellet lifetime can be expressed analytically as

$$\tau = 5.8 \times 10^{-7}\, n_s^o\ n_e(0)^{-0.33}\ T_e(0)^{1.64}\ r^{5/3}. \qquad (5.6\text{-}2)$$

It follows that the speed required to penetrate to the plasma center is given by the ratio of the plasma minor radius to the lifetime as determined by Eq. (5.6-2). The ablation rate is most sensitive to the electron temperature. Higher temperatures imply shorter pellet lifetimes and consequently higher pellet speeds are needed to penetrate a given plasma size. Using larger pellets is a technique that is frequently utilized to obtain central penetration in higher-temperature laboratory plasmas. However, large pellets impose large perturbations on the plasma density. Although increments in excess of 100% have been demonstrated, 20% to 30% global perturbations are more desirable for plasma stability. For an ignited plasma, the perturbation may have to be lower still to avoid quenching the fusion reaction. For a power reactor, the perturbations should be even smaller in order to keep the fusion power absorbed by the in-vessel components and blanket in a near steady-state condition. For this case, the maximum density perturbation per pellet depends on the details of particle and power transport in the plasma and the penetration depth of the pellet. For the ARIES-I fueling analysis, the maximum density perturbation per pellet has been set at 15% during the burn phase. From this increment (15%), the plasma volume ($\sim$500 m^3), and the DT density (1.1×10^{20} m^{-3}), the cylindrical-pellet size is found to be 6 mm in diameter and in length. A 5% fuel change corresponds to 4-mm pellets (the size used in the ARIES-I transport analysis). If sabots are not used, the pellet will have to be somewhat larger at formation due to erosion-type losses during the acceleration process.

According to Eq. (5.6-2), a 4-mm-diam tritium pellet that penetrates to the center of a $T_e(0) \simeq$ 40-keV plasma would evaporate in just about 40 ms and, consequently, pellet speeds approaching 40 km/s would be required to penetrate to the center of a 1.5-m minor-radius discharge. To penetrate beyond the scrape-off layer, much lower velocities (of order 1 km/s) are adequate. During the ramp-up to ignition of ARIES-I, the two-stage pneumatic injector will provide pellets with $\sim$20% to 30% density perturbation at velocities up to 5 km/s into plasmas with electron temperatures that are initially modest compared to burn conditions. This will provide some measure of profile control to the evolving plasma density and possibly reduce the auxiliary power required to initiate the plasma burn phase. In large laboratory plasmas with the present state-of-the-art injectors operating at $\sim$1.5 km/s, central penetration typically occurs for peak temperatures on the order of 2.5 keV. Although the neutral-gas shielding model has been benchmarked in this temperature range, velocity projections based on extrapolation to the 20-keV reactor regimes should be considered only as approximate. Other shielding mechanisms, such as the development of a region of high pressure plasma near the pellet surface that diverts magnetic field lines away from the pellet, are predicted to increase the pellet lifetime by as much as 30% and thereby reduce the velocity requirement proportionately [29].

Pellet ablation calculations have been performed for the reference ARIES-I plasma that include specified plasma profiles for electron density and electron temperature. The electron energy flux is normally the dominant effect even in ignited plasmas. The particular model used is the neutral-gas shielding model. Results are presented in Fig. 5.6-1. It can be seen that pellet velocities in the range of 1 to 5 km/s allow fueling well beyond the edge region, even for central electron temperatures of order 35 keV. Deeper penetration is possible if the magnetic shielding mechanism described above is operative in reactor regimes or if larger pellets can be tolerated by the burning plasma. The penetration shown in Fig. 5.6-1, however, is sufficient to significantly decouple core-plasma fueling from the edge region, which is not possible with gas puffing alone. This allows higher fueling efficiencies and lower tritium inventories since the high hydrogenic fluxes required in the edge for optimum divertor conditions and helium exhaust can be done with deuterium gas puffing while the plasma refueling can be done predominately with DT pellets with controllable isotopic concentration. The pellets may also allow a net impurity flux to the edge region which is difficult to achieve with gas puffing alone.

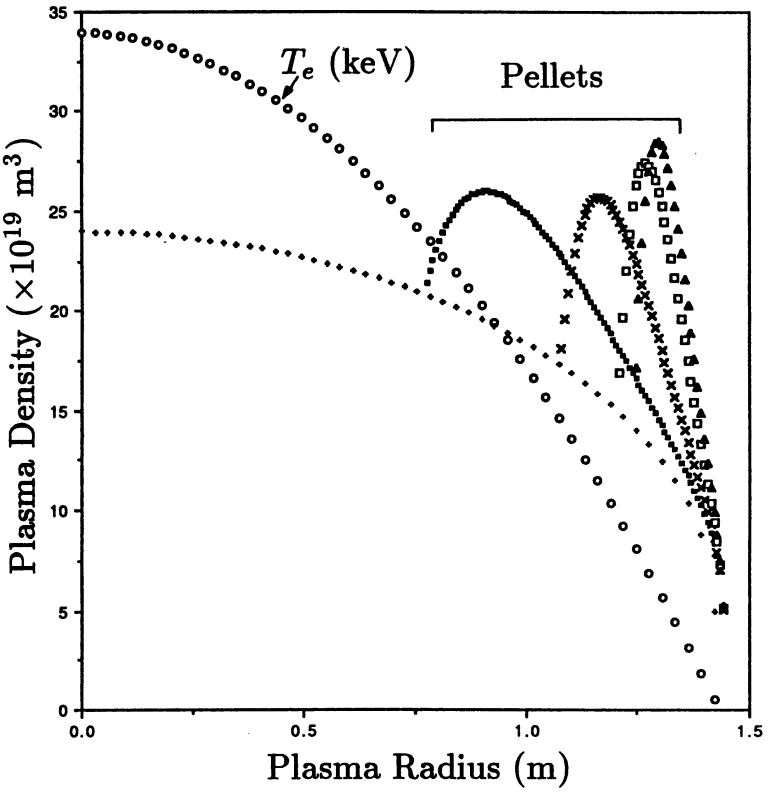

Figure 5.6-1. Pellet penetration and ablation in the ARIES-I plasma for pellet velocities of 1, 1.5, 4.5, and 20 km/s.

5.6.1.2. ARIES-I pellet-fueling specifications

Performance requirements for the ARIES-I pellet-injection system were developed to ensure a sufficient fueling rate for the specified fusion power and fractional burn while minimizing the impact on the isotope reprocessing system and local tritium-inventory levels. Another consideration for this initial fueling-system evaluation was that the supporting technology had to be clearly extrapolatable from present systems to ensure high component reliability in a steady-state fueling system. The technology had to be capable of accelerating repetitive pellets (repetition rate of order 1 Hz) for continuous pulses at high component reliability (of order 90% to 95%). These considerations eliminated some of the more exotic (very high velocity) methods of plasma fueling (such as electron-beam pellet ablation and compact toroid fueling) from consideration, although such systems, at least in a single-shot mode, may be available on the timescale of ARIES-I. The specifications of the ARIES-I pellet-injection system are given in Table 5.6-I.

5.6.2. ARIES-I Pellet-Injection System

5.6.2.1. System description

The pellet injection system comprises three pneumatic pellet injectors: a high velocity (two-stage light-gas gun) injector and two moderate velocity (single-stage light-gas gun) injectors. The parameters of each are given in Table 5.6-II and described below.

1. A high velocity injector will be used with one of the moderate velocity injectors for density ramp-up to ignition. It could also be used for the burn phase if a sufficient piston lifetime is achievable. The second moderate-velocity injector will be used for continuous fueling well beyond the edge region during the burn phase. The moderate velocity injectors are similar and could be used interchangeably, hence providing greater reliability.

2. Barrel diameter accounts for radial growth due erosion loss in barrel. The capability of using pellets of varying sizes is obtained by using two separate light-gas guns in a common enclosure.

3. Barrel diameter accounts for the thickness of sabots. The capability of using pellets of varying sizes is obtained through sabot design.

Table 5.6-I.
ARIES-I Pellet-Injection-System Specifications

Pellet diameter[a] (mm)	4 – 6
Pellet species[b]	H, D, T, DT
Pellet velocity[c] (km/s)	1 – 5
Maximum injection frequency (Hz)	3
Total pellets	
Ramp-up	60
Burn	Continuous
System reliability[d]	97%

[a]Corresponding to 5% and 15% density perturbation per pellet.
[b]Normal species mix is 50:50 DT, but this can be varied.
[c]Low end (1–1.5 km/s) is with a single-stage pneumatic injector (alternate-centrifuge injector); high end is with a two-stage pneumatic injector.
[d]Achieved through combination of pellet injectors.

Table 5.6-II.
ARIES-I Pellet-Injection-System Parameters

	Moderate Velocity Injectors	High Velocity Injector
Pellet speed (km/s)	1 – 1.5	2 – 5
Barrel diameter (mm)	5.0 & 6.72	9.03
Pellet type	H, D, T, DT	H, D, T, DT
Repetition rate (Hz)	0 – 5	0 – 2
Reliability	95%	90%

The moderate-velocity pellet-injection design, similar to the JET pellet injector [31], consists of two single-stage, light-gas guns in a vacuum enclosure. Pellets of different diameters are used because of the ranges of plasma density perturbation per pellet (Table 5.6-I) and of plasma operating densities. The ramp-up to ignition will have a continuously increasing plasma density, and the ignition density will differ in accordance with plasma temperatures and heating profiles. The largest pellet (6.0-mm diam) causes a 15% density perturbation in ARIES-I. For the moderate velocity injector, the diameter of the formed pellet, as well as the barrel, may have to be ~10% to 15% larger than the pellet size listed in Table 5.6-I because of the possible erosion of the pellet material in the barrel during acceleration. Barrel erosion increases with pellet velocity, however, barrel erosion should be small for the velocity range of 1 to 1.5 km/s of the moderate velocity injector. (Tritium and DT pellets are especially vulnerable to excessive tritium loss by barrel erosion). The reliability figures in Table 5.6-II are believed achievable. The JET pellet-injection system has operated for sustained periods at reliability well over 90% [33]. The overall system reliability of 95% will be achieved by improving existing designs and by utilizing the potential overlap (of pellet sizes and repetition rates) between the moderate and high velocity injectors. Thus, the smaller pellet size in Table 5.6-II (5-mm diam) allows fueling rates equivalent to the nominal 6.7-mm pellet if higher pellet-repetition rates are used. Penetration of the pellet into a hot plasma is a strong function of the initial diameter (proportional to $r^{5/3}$) of the pellet, and the largest possible pellet (given the perturbation limits) should be used to provide the most leverage on plasma density-profile peaking. It is well known that peaked density profiles increase the fusion rate and can, therefore, increase the ignition margin even if the plasma transport is unchanged.

The centrifuge pellet injector [34, 35] is an alternative to the moderate velocity injector. This configuration has the advantage of not having a propellant gas load, which eliminates the need for a differentially pumped pellet-injection vacuum line and the reprocessing requirements of a large propellant-gas flow. Experience with this concept indicates that at pellet velocities above 600 to 800 m/s, it is difficult to produce consistently intact pellets, although further research may mitigate the problem. Currently, however, the larger pellet size required by ARIES-I may amplify this effect because of the larger free surface during the acceleration phase. Pneumatic gun barrels constrain the pellet in two dimensions during the acceleration phase, which is not possible in the rim of a centrifuge arbor. Thus, centrifugal injectors remain an option for fueling beyond the scrape-off layer and the performance of the recently installed centrifugal injector on the Tore Supra should be evaluated for future ARIES-I application. An open question in the trade-off between the centrifuge and pneumatic approaches for the moderate velocity injector is the benefit provided by the additional 400 to 800 m/s offered by single-stage

pneumatic injectors. This incremental velocity is substantial in the warm, outer plasma region and the implications of this additional penetration need to be evaluated. Finally, it should be mentioned that the present level of effort in developing the centrifuge injector concept is quite small.

The high-velocity pellet injector is based on the two-stage light-gas-gun concept [36] where a piston is pneumatically accelerated in a high-pressure pump tube and provides an adiabatic compression of a propellant gas between the piston and the pellet/sabot. The resulting high pressures (up to 6,000 bar) and, more importantly, high temperatures (up to 4,000 to 8,000 K) can accelerate the pellet/sabot payload to muzzle velocities in the 4- to 5-km/s range. Explosively driven pistons have accelerated heavy kg-size projectiles to speeds above 6 km/s in single-shot, two-stage light-gas guns. For the pellet/sabot combinations used for ARIES-I, the accelerated mass is typically <0.5 g and the mass per unit area is <7.5 kg/m^2. This permits consideration of repetitive operation since the pump tube conditions are moderate enough to allow multiple shots with a single piston. The sabots are separated from the hydrogenic pellets in the injection line to the torus and allowed to impact a ruggedly designed target plate. Two-stage light-gas-gun pellet injectors are under development at Oak Ridge National Laboratory and in Europe [31,37–40].

5.6.2.2. System layout

A plan view of the pellet injector installation is shown in Fig. 5.6-2 and extrapolated from the proposed ITER pellet-injection system. The two-stage high-velocity injector is located on the centerline of a vacuum vessel port at approximately 24.5 m from the center of the ARIES-I reactor. The moderate velocity injectors are on either side of the two-stage pneumatic injector such that the centerlines of the three injectors converge in the mid-plane at a major radius of 6.0 m. To prevent the propellant gas from reaching the torus, the injectors are isolated from the vacuum vessel by a series of three separately pumped vacuum chambers connected by conductance-limiting pellet guide tubes and flow-limiting fast-acting valves. The pellet injector bay is shielded by the structural shielding wall, by a rotating eccentrically bored shielding drum in each injection line (to limit line-of-sight exposure of the injectors), and by modular shielding around the high-vacuum isolation chamber. The bay also serves as a redundant containment boundary and is sealed by bellows at the shielding wall and by an airlock at the entrance. The walls, floor, and ceiling of the bay will be sprayed with a peelable compound that can be removed and replaced in the event of tritium contamination. Equipment in the pellet

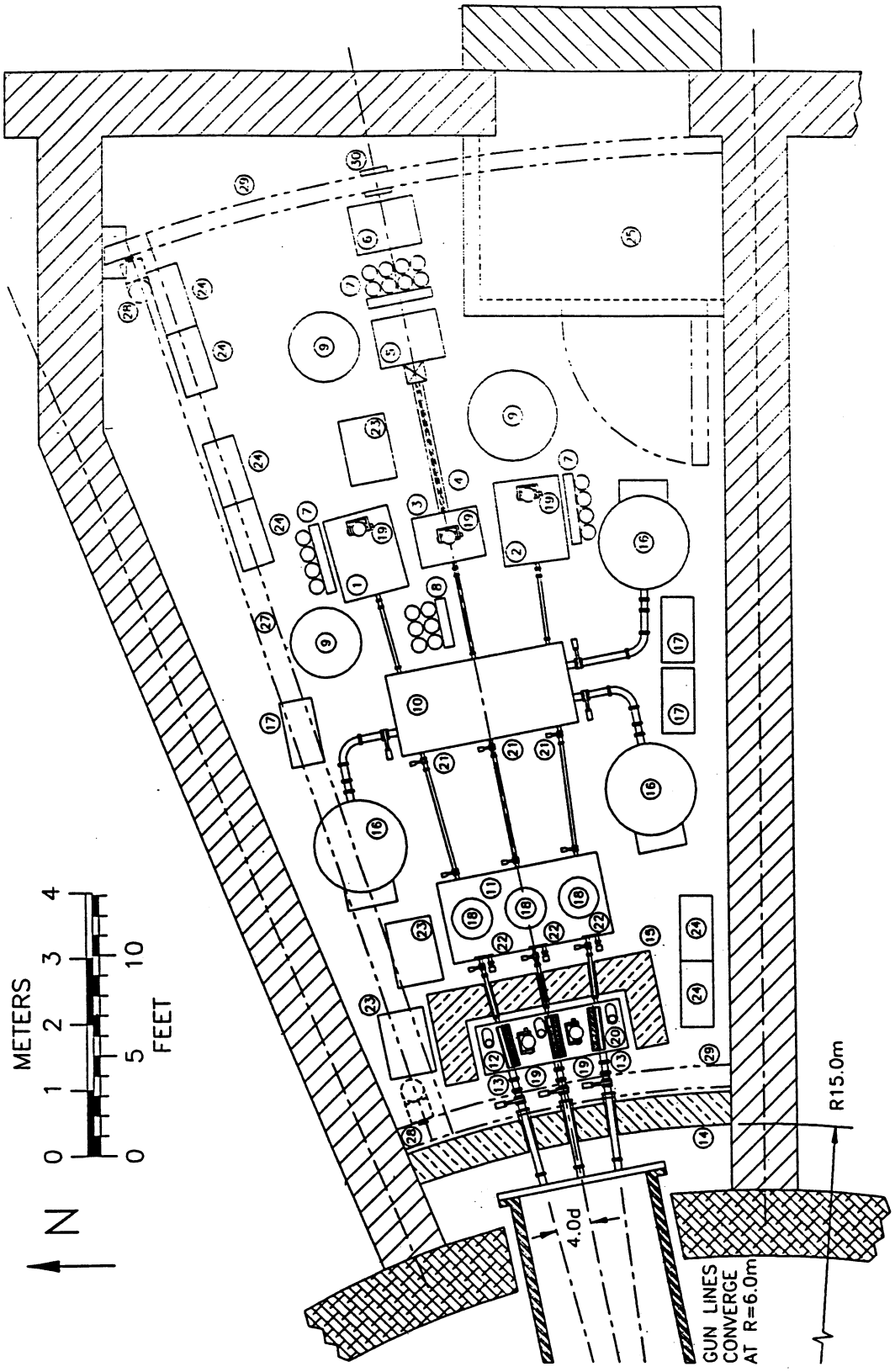

Figure 5.6-2. Plan view of the ARIES-I pellet-injection system showing the moderate (1 & 2) and high velocity (3) injectors, the propellent system (5 – 8), the vacuum chambers (10 – 12), and pumps (16, 18, & 19).

injector bay is serviced by a 10-ton crane and a bridge-mounted articulated manipulator supported on curved rails at machine radii of approximately 15.7 m and 29.5 m.

5.6.2.3. Single-stage light-gas-gun analysis

A gas gun operates on the principle that a projectile confined laterally in a tube or gun barrel will experience an acceleration when subjected to an applied pressure imbalance. When the fluid that supplies the driving force is a compressible gas, the projectile can be accelerated to high speed as the internal energy of the gas is converted in the expansion process to kinetic energy of the projectile.

The performance of the basic, single-stage light-gas gun can be modeled analytically [41] by assuming that the pellet accelerates in an infinite tube of constant cross section. The motion of the pellet is then governed by the propagation of simple rarefaction waves into the high pressure medium [42]. Neglecting non-ideal effects such as friction at the projectile/tube interface, heat transfer, and viscosity, the pellet velocity, $U(t)$, at time, t, after the sudden application of the gas at pressure, P_o, is given by

$$U(t) = \frac{2C_o}{\gamma - 1}\left\{1 - \left[1 + \frac{(\gamma+1)\,A_p}{2M\,C_o}\,P_o\,t\right]^{-(\gamma-1)/(\gamma+1)}\right\}, \qquad (5.6\text{-}3)$$

where C_o is the propellant-gas sound speed, γ is the ratio of specific heats, M is the projectile mass, and A_p is the projectile base area.

Equation (5.6-3) illustrates several important points concerning the acceleration of the hydrogen isotopes. First, high performance is possible with relatively low forces (pressures) since the projectile mass is small. Secondly, a high sound speed is required for high speed operation, which favors low molecular-weight gases and high temperature. A study of the effects of propellant gases of different mass and temperature on performance was reported [43]. It was found that warm hydrogen at 400 K provided about a 30% improvement relative to room temperature helium. Other studies of propellant gas heating have not been conclusive and this approach to incremental performance gain is not recommended for ARIES-I. The effect of pellet mass was also studied [44] and it was found that the performance with deuterium is reduced by about 15% relative to the lighter hydrogen pellets. Recent experiments with tritium pellets performed by Fisher *et al.* [45] (Fig. 5.6-3) show a similar reduction relative to the deuterium data.

The data of Fig. 5.6-3 and results from other studies [46] generally agree with the predictions of Eq. (5.6-3) (the ideal gun theory) to within 80% [47]. These data show

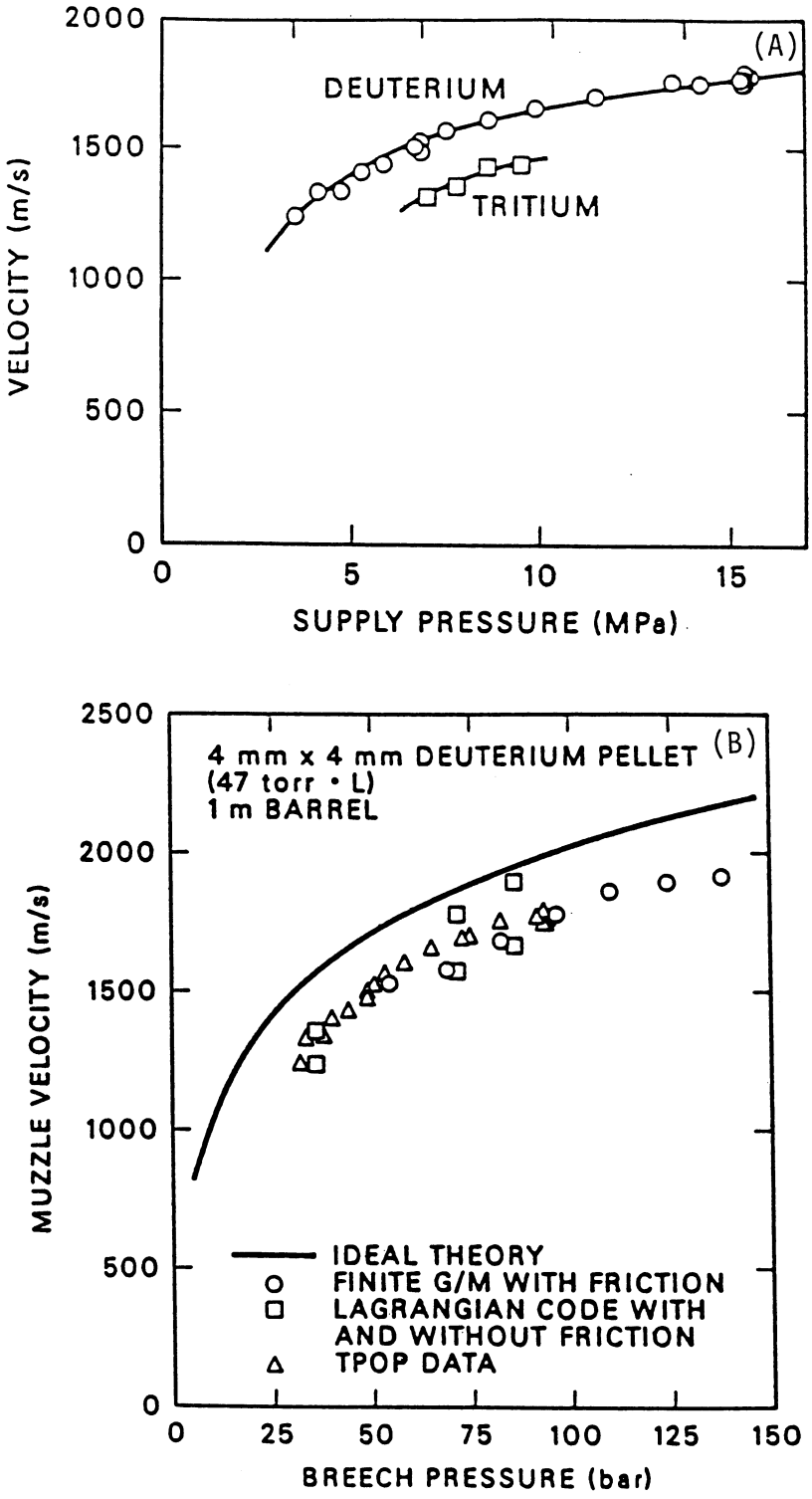

Figure 5.6-3. (A) Pellet velocity as a function of the supply pressure for deuterium and tritium pellets. (B) Deuterium-pellet velocity data and theoretical results.

a saturation in velocity at about 2 km/s, which is because the pellet is traveling at speeds greater than the local sound speed. At velocities above $\sim 1.5\, C_o$, pressure pulses emanating from the breech of the gun can not propagate quickly enough in the cold gas that fills the barrel. Consequently, the pressure at the base of the pellet, which is responsible for the acceleration, is reduced substantially below the breech pressure, P_o. For this reason, single-stage light-gas guns are generally limited to pellet speeds slightly in excess of 2 km/s. As we shall see later, this limitation is overcome in two-stage light-gas guns where higher accelerations are maintained by increasing the temperature of the propellant by rapid adiabatic compression of the gas at the breech.

The pellet feed in a repetitive pneumatic gun is generally accomplished with cryogenic extruders that are generally capable of moving solid material at a sufficiently high rate of speed ($\sim$5 cm/s) to provide a "real-time" pellet-feed system. The apparatus shown in Fig. 5.6-4 is an example of a repeating pneumatic injector [44] that is capable of delivering pellets continuously at rates of up to 5 Hz. The injector developed for the JET [31,34] tokamak features three units of 2.7-, 4-, and 6-mm capability in a common vacuum enclosure. This versatile device consists of three independent, machine-gun-like mechanisms that operate at cryogenic temperatures (14 to 20 K). Individual high-speed extruders provide a continuous supply of solid deuterium to each gun assembly, where a reciprocating, electromagnetically driven, breech-side cutting mechanism (punch tube) forms and chambers cylindrical pellets from the extrusion; deuterium pellets are then accelerated in the gun barrels to velocities $\leq$ 1.5 km/s with controlled amounts of compressed hydrogen gas delivered by fast electromagnetic valves.

Each gun is capable of operating (individually or simultaneously) at the design repetition rate for 15-s duration pulses (limited only by the capacity of the extruder feed system). The extruder section consists of a liquid reservoir positioned above a cylindrical freezing chamber that is fitted at its outlet with a tapered, copper extrusion nozzle. A programmable motor-driven screw press activates a piston that moves vertically inside the cylindrical bore of the freezing chamber where the solid deuterium charge is located. The extrusion nozzle, which terminates just above the chambering mechanism position, provides a smooth transition from the 10.5-mm cylindrical extruder bore to a rectangular-like cross section whose length is larger than the punch tube diameter and whose width determines the length of the pellet. Present deuterium extruders typically operate at $\sim$14 K where the shear strength of the ice is sufficiently low to prevent excessive piston forces at high extrusion rates.

The extruder system described above, with modifications to provide tritium-compatible materials and a minimum tritium-waste stream, will suffice for the injectors used for

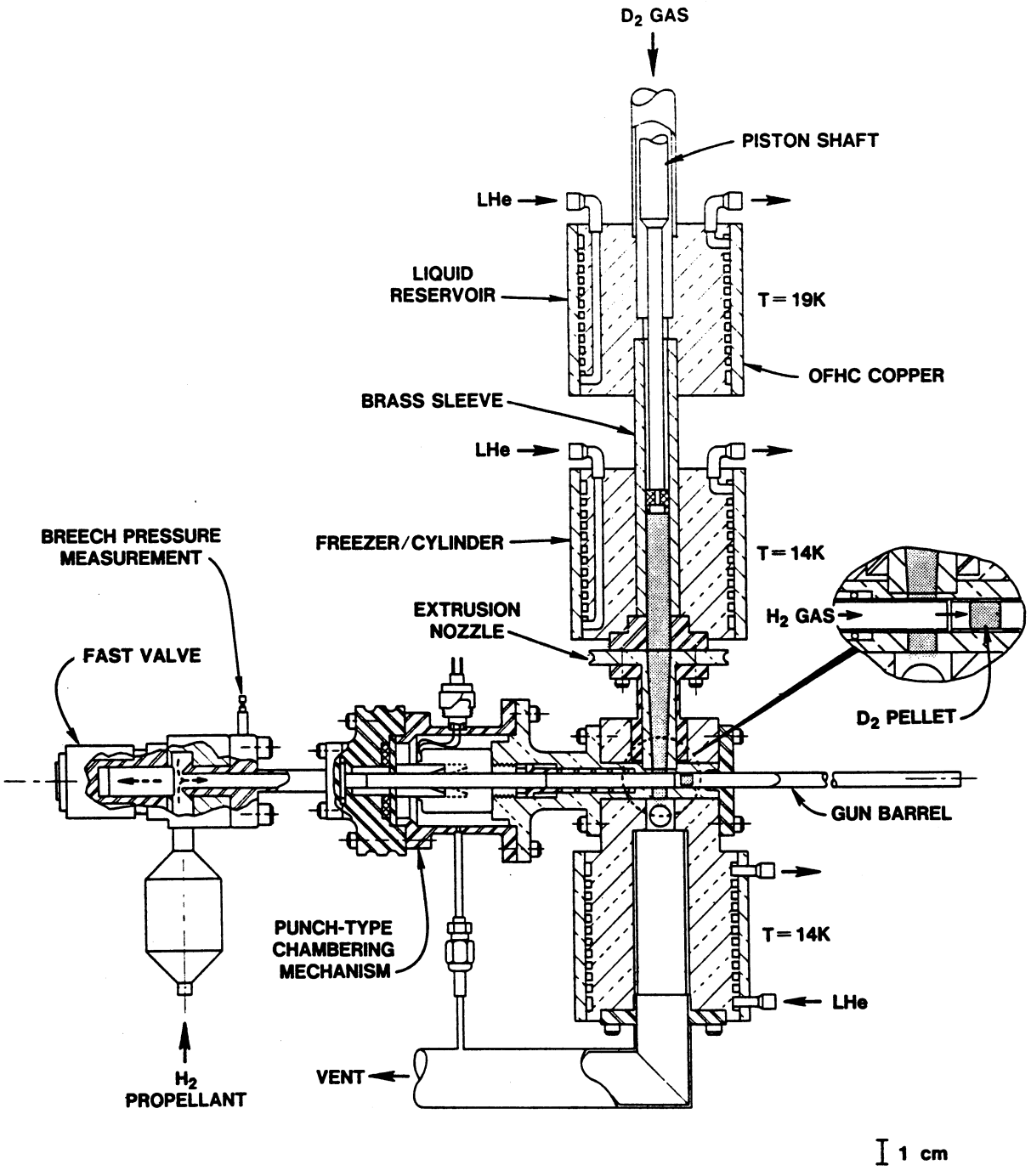

Figure 5.6-4. Schematic of a repeating pneumatic injector.

plasma ramp-up to ignition. The continuous injector for the burn phase will require a steady-state extruder system, such as the double extruder system proposed by the Leningrad Polytechnical Institute, that allows one extruder to be refreshed while the other is extruding pellet feed material. Another variant is a rotary extruder with synchronized valves to allow extrusion and refreshing at different locations. Extruder development is required for ARIES-I.

An analysis of the performance of single-stage light-gas guns for ARIES-I has been carried out using two methods: (1) generic light-gas-gun curves developed by A. E. Seigel [48] and (2) numerical calculations using a Lagrangian finite-difference code [47]. The generic, dimensionless curves developed by Seigel were made by using both the method of characteristics and a Lagrangian code with no losses. The Lagrangian finite-difference code has the following capabilities for modeling either single-stage or two-stage light-gas guns: (1) Lagrangian formulation of the finite-difference representation of the 1-D differential equations of continuity, motion, and energy; (2) shocks which form in the pump tube and barrel are treated by the artificial viscosity method of von Neumann and Richtmyer which spreads out shocks due to dissipative effects such as viscosity and heat conduction; (3) the code can model either real (variable specific heat) or ideal gases; and (4) non-ideal effects (*e.g.,* piston friction and plastic deformation, heat transfer from gas to wall, and smooth-wall or constant-factor gas friction) can be included.

When the code was used in the single-stage pneumatic mode to model TPOP injector data, best agreement was obtained by using the ideal gas equation of state with gas friction [see Fig. 5.6-3(B)]. Runs made with the two-stage version of the code show gas friction to be the dominant non-ideal effect with heat transfer and piston friction accounting for only 10% of the energy loss relative to that due to gas friction. This conclusion agrees with recent theoretical work at the RISØ National Laboratory in Denmark.

As mentioned earlier, the pellet size is determined by providing a 15% density perturbation per pellet, corresponding to a 6.0×6.0-mm right circular-cylinder DT pellet. For a single-stage light-gas gun operating without sabots, the pellet size would be 6.7×6.7 mm and the DT pellet would weigh 0.059 g. Results from the code runs, presented in Table 5.6-III, show that the velocity goal of 1 to 1.5 km/s is achieved. The maximum pellet acceleration for the bare pellet is within acceptable limits. For 6.0-mm pellets, the pellet repetition rate is about 1 Hz and the propellant gas load is $\sim$700 mbar-l/s.

It should be noted that the use of sabots to limit erosion losses for the single-stage light-gas gun slows the pellet down to near 1 km/s where barrel erosion is probably not significant. A saboted pellet for the single-stage light-gas gun is not desirable for the

Table 5.6-III.
Single-Stage Pellet-Injector Parameters

Pellet speed (km/s)	1.48
Projectile mass (g)	0.059
Barrel diameter (mm)	6.7
Barrel length (m)	1.25
Breech length (m)	0.20
Propellant gas load (mbar-l)	710
Repetition rate (Hz)	0 – 5
Maximum acceleration (m/s^2)	6.0×10^6

following reasons: (1) the propellant gas load is significantly increased (2.5 times) and the muzzle velocity is 30% lower for the sabot case; (2) the use of sabots limits the repetition rate to a few Hz which decreases flexibility; (3) the problem of sabot separation after a pellet/sabot exits from the barrel increases the complexity of the device; and (4) since the single-stage injector will be used in the continuous burn phase, the use of sabots at a repetition rate of 1 Hz generates significant tritium-contaminated waste.

5.6.2.4. Two-stage light-gas-gun analysis

As shown above, it will be difficult to accelerate DT pellets with a weight of order 100 mg to speeds above 1.5 to 2.0 km/s with single-stage, room-temperature-propellant, pneumatic guns. To achieve muzzle velocities in the range 2 to 5 km/s requires raising the temperature (sound speed) of the propellant gas at significant pressure levels. A straightforward way of doing this is possible by using two-stage pneumatic light-gas guns. This concept, developed in the late 1940s by W. D. Crozier [36], was refined over the next 25 years, and is today the major method for hypervelocity research at the major defense and aerospace facilities. The main reason for its longevity is the basic simplicity of the concept. Propellant gas at moderate pressure (30 to 100 bar) accelerates a plastic,

metallic, or composite piston (mass 30 g to a few kg) to velocities in the range of 100 to 350 m/s in a high-pressure, thick-walled pump tube. The low pressure gas (H or He at ~1 bar) on the other side of the piston is initially at room temperature and is subsequently adiabatically compressed to high temperature and pressure and becomes the driving gas for the projectile. At this higher pressure, the mechanical strength of the hydrogenic pellet becomes a design constraint and the peak pellet acceleration must be controlled.

Single-stage pneumatic guns typically have peak pellet-acceleration values in the range 1 to 8×10^6 m/s^2 for barrel lengths of order 0.5 to 1.0 m. By carefully controlling the pellet formation process and temperature, it is possible to accelerate consistently intact pellets in this acceleration range. Initial experiments to accelerate hydrogenic pellets with two-stage light-gas guns are described in Refs. [32,37–40]. These experiments report peak acceleration levels in the range 5 to 6×10^6 m/s^2 without pellet breakup. This is somewhat lower than pellet acceleration values inferred from the best pellet performance in single-stage guns. For example, the TPOP data [Fig. 5.6-3(B)] had inferred peak acceleration values for deuterium pellets near 10^7 m/s^2 at the higher breech pressures, which agrees well with peak acceleration computed by the Lagrangian code with smooth-wall gas friction. In designing a two-stage gun, it will be necessary to limit the peak pellet acceleration to levels around 6 to 8×10^6 m/s^2 if sabots are not used. Higher acceleration levels would be feasible with sabots, and initial efforts [32] with unoptimized plastic sabots encasing deuterium pellets were accelerated to muzzle velocities of 3,400 m/s. The sabots also limit erosion of the pellet diameter, which becomes an issue at higher velocities. Two complications introduced by sabots are the separation of the sabot from the pellet and the sabot impact on a suitable target material. These become more critical for a repeating pellet injector where eventual steady-state operation is desired for fusion-reactor-scale devices.

A two-stage gas-gun arrangement suitable for ARIES-I is shown in Fig. 5.6-5 and its parameters are given in Table 5.6-IV. This gun comprises (1) the first stage reservoir containing about 4.8 liters of hydrogen gas at a pressure between 30 and 100 bar, (2) a plastic-metallic composite piston of mass 217 g and mass density 2,000 kg/m^3, (3) a cylindrical pump tube (the second stage) of 2.5-m length filled initially with hydrogen propellant gas at 1.1 bar pressure, and (4) a cryogenic extrusion and sabot-positioning apparatus which serves as the cryogenic pellet source. In Fig. 5.6-5, the first and second stages are separated by a repetitive fast valve. The friction between the tight fitting sabot and the barrel determine the breakaway pressure (typically 20 to 70 bar) of the projectile.

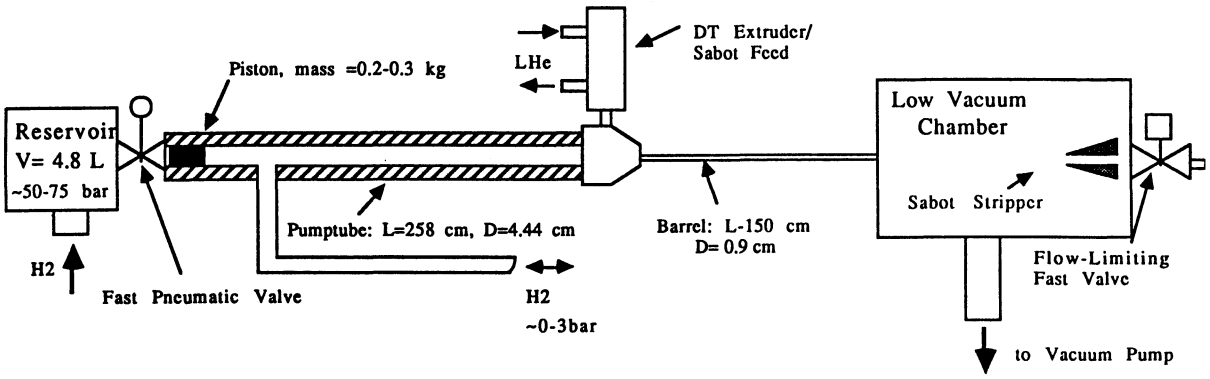

Figure 5.6-5. ARIES-I two-stage light-gas gun.

Present systems operate at up to 2.8 km/s with unprotected deuterium pellets [38]. The speeds have been limited by a progressive reduction in the pellet diameter, thought to be caused by erosion by the gun barrel wall, which becomes important at speeds >2 km/s [32]. Speeds as high as 3.8 km/s have been achieved by encasing the pellet in a sabot [32,40]. With sabots, the pellet can withstand the higher acceleration rates imposed by the two-stage gun and is protected from the effects of erosion. Sabots that separate from the pellet after it exits the muzzle are being developed in the U.S. and in Europe. To maximize performance of a two-stage gun, it is necessary to maintain the pellet acceleration as close as possible to the pellet or sabot fracture limit throughout its travel through the gun barrel. This is essentially the constant base-pressure approach discussed by Seigel [48]. The two-stage concept is potentially attractive for approaching roughly constant base pressure because of the ability to control pump tube conditions by varying the first-stage pressure input, initial pressure in the second stage, and piston mass density.

Using the Lagrangian code discussed in Sec. 5.6.2.3, the performance of an ARIES-I two-stage light-gas gun was studied. Inputs and outputs of the code are summarized in Table 5.6-IV. The pressure behind the projectile and piston velocity, as well as the projectile velocity and acceleration as functions of distance along the barrel, are shown in Fig. 5.6-6.

Table 5.6-IV.
Two-Stage Light-Gas-Gun Code Results

Code Inputs	
Pellet/sabot mass (g)	0.4
Piston mass (g)	217
Piston density (g/cm^3)	2
First stage pressure (bar)	54.8
First stage volume (liter)	4.8
Second stage (pump tube) pressure (bar)	1.1
Pump tube length (cm)	258
Pump tube diameter (cm)	4.44
Barrel length (cm)	150
Barrel diameter (cm)	0.90
Propellant gas	H
Sabot release pressure (bar)	70 bar
Code Outputs	
Pellet velocity (m/s)	4,700
Peak pellet/sabot acceleration (m/s^2)	3.2×10^7
Peak pump-tube pressure (bar)	5,800
Peak pump-tube temperature (K)	~3,000
Maximum piston velocity (m/s)	315
Two-stage active pulse length (ms)	13

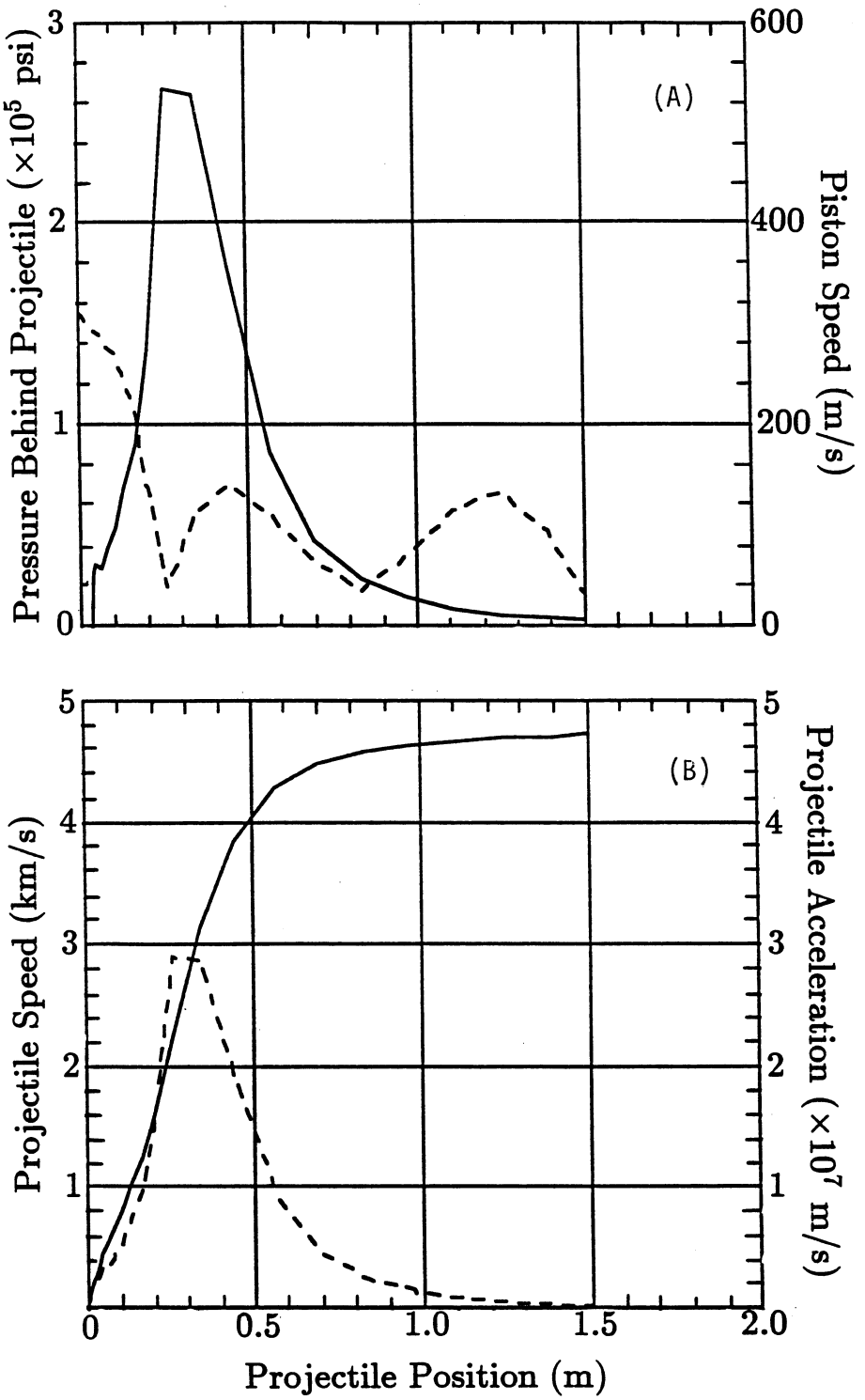

Figure 5.6-6. Performance of the ARIES-I two-stage light-gas gun: (A) pellet accelerating pressure and piston velocity and (B) pellet velocity and acceleration as functions of pellet location in the barrel.

The performance of this gun meets the velocity objective of 4 to 5 km/s while keeping propellant gas loads to reasonable levels. While modeling the two-stage light-gas-gun dynamics, variations in gun geometry, piston mass, and initial gas pressures were evaluated. The constraints were to meet the velocity objective while keeping the peak pump-tube pressure less than about 7000 bar in a reasonable sized system to minimize propellant gas loads. This problem is nonlinear and progress towards a design point is done by computational iteration aided by guidelines from experimental data in prototypical systems. Performance (muzzle velocity) is not strongly affected by piston mass once an optimum pump-tube length and initial pump-tube pressure have been chosen. The piston mass and initial first-stage (reservoir) pressure have been varied to meet the above-mentioned constraints. Increasing the first stage pressure always results in increases in muzzle velocity, maximum piston velocity, and maximum pump-tube pressure. Changing the piston mass can actually result in a higher pump-tube pressure as the muzzle velocity decreases because the dynamics at the end of the pump tube are coupled to the pellet dynamics through the specified breakaway pressure of the pellet/sabot. (This can be set by providing a shear lip on the back circumference of the sabot.) The current goal of the development program is to produce a system with maximum repetition rate in the 1- to 2-Hz range, which is more than adequate for ARIES-I.

5.6.2.5. Pellet injection line

The pellet injectors use a light gas to accelerate the pellets and a design consideration is to ensure that only a low amount of propellant gas is introduced into the vacuum vessel. For the high velocity injector, sabots are required because of the large initial accelerations of the low-strength hydrogen ice. Pellets accelerated by the moderate velocity injector, however, will not be encased in a sabot. These pellets will experience some erosion due to contact with the barrel (in the range of 10% to 40%, depending on the pellet velocity). For ARIES-I, with a likely velocity in the range of 1 to 1.5 km/s, a conservative mass loss of 30% due to erosion is assumed. Therefore, the propellant gas is contaminated with tritium and has to be stored or recycled.

For pneumatic injectors, there are three potential light gases for pellet acceleration: hydrogen, deuterium, and helium. The sound speed, C_o, and escape velocity, v_e, are defined as

$$C_o = \left(\frac{\gamma R T}{M}\right)^{1/2}, \tag{5.6-4}$$

$$v_e = \frac{2}{\gamma - 1} C_o, \tag{5.6-5}$$

where γ is the ratio of specific heats, T is the gas temperature (room temperature for the moderate velocity injector), M is the gas molecular weight, and R is the universal gas constant. The escape velocity, which is never attained in practice, is that velocity attained by a projectile undergoing an ideal isentropic acceleration when the gas pressure behind the projectile decreases to zero. Both of these parameters are figures of merit for the choice of gas in pneumatic injectors. Hydrogen gas has the highest sound speed (1310 m/s) and escape velocity (6551 m/s). For this reason, hydrogen is normally used for the propellant gas in light gas guns. Helium is also used occasionally because it is complicated to design exhaust systems to eliminate excessive hydrogen concentrations. However, for ARIES-I, because the on-site reprocessing system can accommodate tritium-contaminated hydrogen streams efficiently, it was decided to use hydrogen as the propellant gas since it gives the best performance in terms of muzzle velocity. The relative reductions of pellet muzzle velocity at a given propellant-gas pressure for hydrogen, deuterium, and helium are shown in Fig. 5.6-7. The muzzle velocities on the vertical axis are from ideal gun theory and, in practice, higher breech pressures would be required for a given muzzle velocity.

Because the leakage rate into the ARIES-I vessel is specified at 0.1 mbar-l/s and the propellant gas (H) is an impurity for D and DT plasmas, a value much smaller than the propellant gas load used to accelerate the pellet. For the ARIES-I reactor, the refueling rate is $\sim 5 \times 10^{21}$ DT molecules/s. With an erosion mass loss of 30%, this requires injection of 6.7 × 6.7-mm cylindrical DT pellets at a rate of about 1 Hz (for a plasma density perturbation of 15% per pellet). Hydrogen-propellant gas per pellet of order 710 mbar-l/s is required for the single-stage pneumatic injector. Figure 5.6-8 is a schematic of a differentially pumped, vacuum-injection line that uses tritium-compatible vacuum pumps and limits the hydrogen propellant gas to the ARIES-I vessel to significantly less than 0.1 mbar-l/s. To accomplish this goal, the pellet injectors are isolated from the torus by a series of three separately pumped vacuum chambers connected by conductance-limiting pellet guide tubes and flow-limiting fast-acting valves (Figs. 5.6-2 and 5.6-8). Most of the propellant gas is pumped by the Normetex scroll pumps at the low vacuum chamber. A fast-acting valve on the down-range side of this chamber opens for a small fraction of a second to allow the pellet to pass, and some of the propellant ($\sim$10 mbar-l/s) escapes to the mid vacuum chamber where most of it is pumped by three 5000-l/s turbomolecular pumps. A very small amount (<0.01 mbar-l/s) of the gas in the mid vacuum chamber escapes through the guide tube to the high-vacuum chamber, where it is pumped by two 500-l/s turbomolecular pumps. From the high-vacuum chamber, <0.005 mbar-l/s of the gas escapes to the torus. This design includes one redundant pump at each of the three chambers so that a single pump failure will not prevent operation of the injectors.

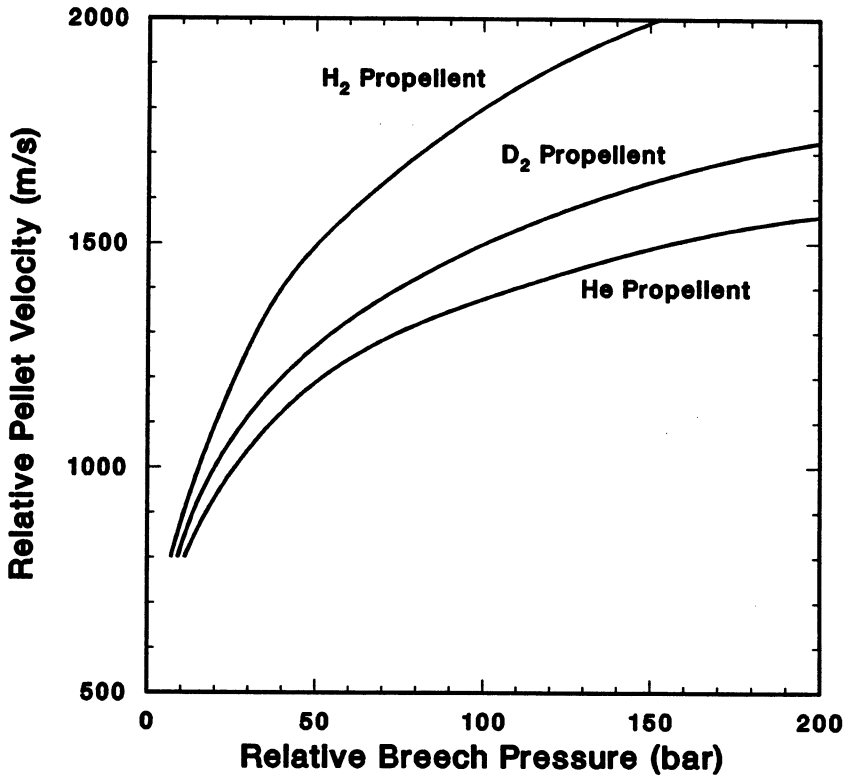

Figure 5.6-7. Projectile velocity as a function of breech pressure for three light-propellant gases.

5.6.2.6. System gas flows

The ARIES-I pellet-injection-system gas flows are given in Table 5.6-V. The design column is an estimate of requirements for the reprocessing system and includes some conservatism for current unknowns and future flexibility. The actual value of hydrogen contamination of excess DT from the extrusion process is not well known. Because the DT contamination will probably be no more than a few %, this stream could be processed separately from the propellant gas stream which is predominately hydrogen. Although the first-stage propellant load of the two-stage injector is substantial, tritium contamination may be low so a local recycle and compression may be feasible. Deuterium-tritium levels of 0.1% to 1.0% in the recycled propellant gas are feasible without much effect on ballistic performance; a limiting factor may be the amount of tritium inventory tied up in the recycled hydrogen propellant gas.

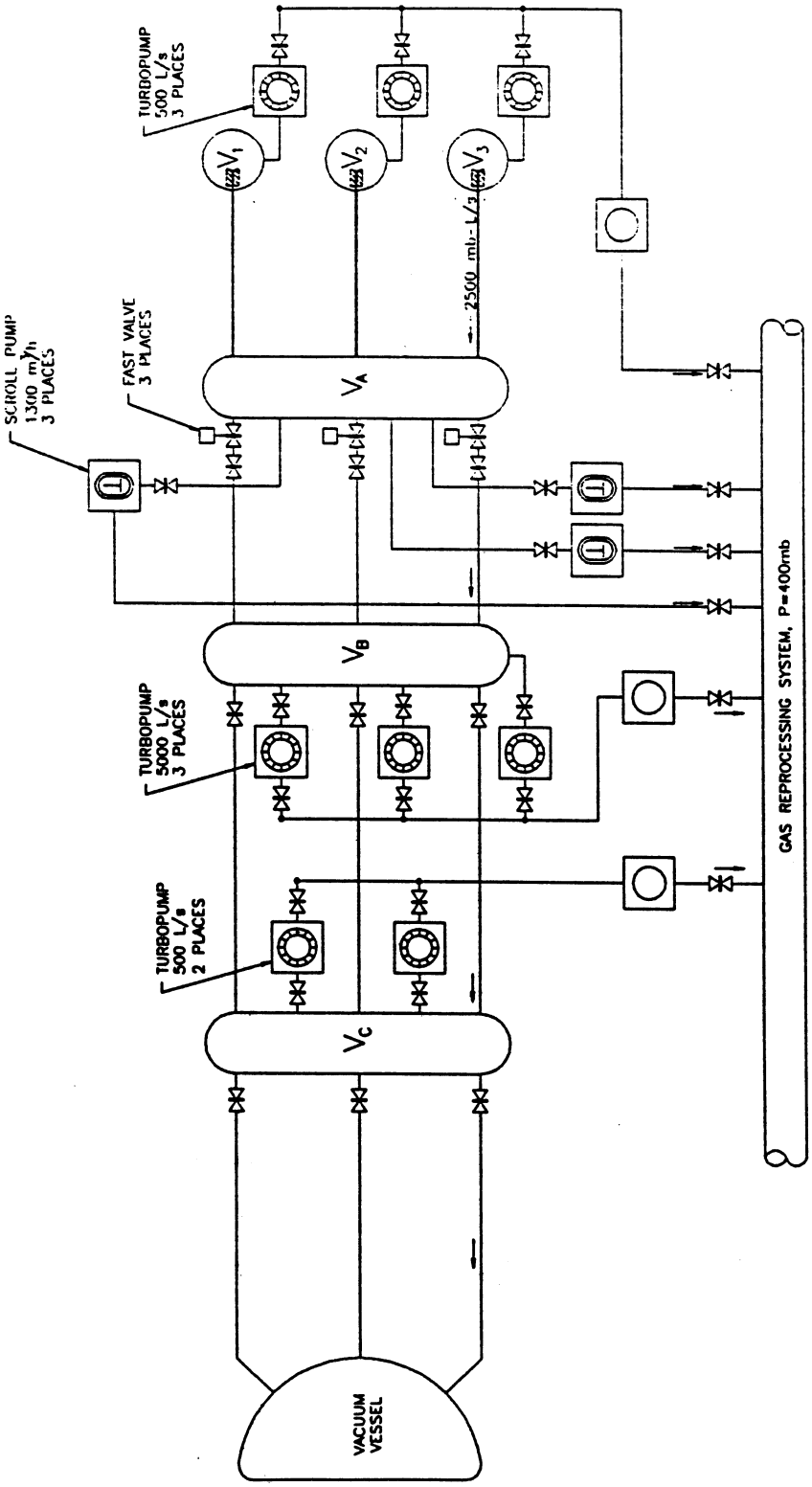

Figure 5.6-8. Differentially pumped pellet-injection line for ARIES-I.

Table 5.6-V.
Pellet-Injection-System Flows (mol/h)[a]

	Without Sabot	With Sabot	Design Value
Single-stage pneumatic injector[b]			
H_2 propellant gas	78		150
DT to torus	22		40
Excess DT from pellet formation[c]	32		60
DT in propellant gas	10		20
Two-stage pneumatic injector[d]			
H_2 propellant gas			
Single stage[e]	2,000	2,000	4,000
Two stage[f]	26	26	50
DT to torus	2.4	2.4	5
Excess DT from pellet formation[c]	4.8	2.64	10
DT in propellant gas[g]	2.4	0.24	5

[a]Desired purity of returned mole fraction DT $< 0.1\% - 1.0\%$ propellant gas.

[b]Based on continuous operation.

[c]From the extruder feed; should be fairly pure (*i.e.*, little H_2 contamination).

[d]Used during plasma start-up; assumed production of 30 pellets every 12 minutes (*i.e.*, 5 tokamak pulses per hour).

[e]Isolated from the DT pellet by a yet-to-be-developed piston cylinder seal; only slight contamination by DT and could be recycled locally at the pellet injector.

[f]Similar to a single-stage gas stream because it is from the barrel muzzle and, therefore, could be contaminated with DT.

[g]Based on 50% mass loss at velocities of 2 to 2.5 km/s.

Liquid helium will be used to cool the extruders and maintain design temperatures of 14 to 15 K for the DT ice. Actual consumption rates will depend on the specific design of the system including heat shielding, reflecting surfaces, and optimum use of the cold waste stream to minimize consumption. The liquid helium system will be a closed system and consumption will be small compared to the magnet loads. Existing systems typically consume 15 to 25 l/h and ARIES-I consumption should be of order 100 l/h.

5.6.2.7. Neutron activation and maintenance approach

In principle, injector component activation can be low because of the small-diameter (few cm) guide tubes used for pellet transport in the vacuum injection line [49]. The neutron flux to injector components may be reduced to tolerable levels for limited hands-on maintenance by using shielding around the guide tubes, a shielded isolation valve when the injector is idle, a rotating synchronized neutron-shield plug for the continuous injector, and perhaps a slight curvature of the guide tubes to eliminate direct line-of-sight to the vacuum vessel.

Limited hands-on maintenance of most injector components appears feasible but a specific neutronics calculation is needed to quantify this with reasonable exposure times for normal and corrective maintenance. A design goal is to maintain the capability of hands-on maintenance for all components beyond the modular shielding wall (Fig. 5.6-2). Several components will require remote maintenance or replacement: (1) the torus vacuum isolation valve and adjacent bellows, and the ceramic break in each injection line (item 13, Fig. 5.6-2) and (2) the turbomolecular vacuum pump and the drive motor assembly for the rotating neutron shield located near the high-vacuum chamber (items 19 and 20, Fig. 5.6-2).

Other components will be designed to be remotely disconnected and removed through the airlock to a hot cell in the event they become contaminated or activated. Since the shielding drums, synchronized with the pellet firing rate, will minimize activation of injector components, it should be possible to enter the pellet injector bay without protective clothing after purging the tritium lines. In the event of a tritium release, it may be necessary for technicians to wear protective suits. The remote manipulator, equipped with dual replaceable endeffectors and a television camera, will be mounted at the end of an articulated arm attached to a bridge-mounted turret. This will allow manipulator access to all areas of the pellet injector bay and will minimize interference with crane operations.

5.6.2.8. Component reliability

Reliability is a prime design consideration and is achieved through injector and support component redundancy, hardware development including prototyping, and a validated operational history of pellet injectors on TFTR, JT-60, Tore Supra, JET, and a number of smaller confinement devices. The reliability success of the JET injector [33] is the product of a repeating-pneumatic development program, an operational prototype on TFTR in 1985, a rigorous design-review and quality-assurance program, attention to detail, and a well-conceived computer-control system with interlocks. The reliability goal of each of the moderate velocity injectors is 95% and the more complex two-stage injector is 90%. This results in an overall system reliability over 97%.

5.6.2.9. Safety and tritium containment

Since all injectors will have tritium or deuterium-tritium mixtures in the gas fuel supply, it is proposed to provide three layers of containment throughout the pellet injection system. The primary level of containment will be the pellet injector itself which will have tritium-compatible materials throughout. This includes feed lines to the hydrogenic extruders, the extruders, the pellet forming mechanism, the breech/barrel assembly, the pellet injection line, and the interface to the ARIES-I fusion power core. The second level of containment is the tritium isolation boundary defined by the pellet injection room inside the reactor building and double-walled piping for all penetrations of this boundary. The third level of containment is the ARIES-I reactor building itself.

The major decision point in the conceptual design process was how to implement the second or middle level of tritium containment. For small to moderate size components this has usually been done with commercial or custom-designed glove boxes. One advantage of this approach is that a leak in the first level of containment can normally be repaired using the gloves. It is also straightforward to leak check and decontaminate a glove box. However, for a large number of interconnected bulky components, glove boxes become less attractive. As can be seen from Fig. 5.6-2, this is the case for the ARIES-I pellet-injection system. In some cases, the physical dimensions are large enough that a glove may not be able to reach the interior of the component for repairs. Large, custom-designed glove boxes would be required for most of the components. It was, therefore, decided to implement a global room-type boundary. This requires an airlock sized for the largest component and a detritiation system sized for the room volume (the ARIES-I building detritiation system may be used for this purpose if suitable piping arrangements

are made). It also means that if there is a leak of the primary tritium boundary, access to the room will require "spacesuits."

The major energy sources in the system are the stored energy in the high-pressure propellant gas and the kinetic energy of the piston and sabot in the two-stage pneumatic injector. The gas will be recycled but with a working inventory of about 3500 bar-liter, the stored energy of the hydrogen propellant gas approaches 1 MJ. The piston kinetic energy is in the 10 to 20 kJ range and the sabot has a kinetic energy in the range 4 to 8 kJ. The components in the two-stage pneumatic injector and the gas storage and transfer manifold will be designed to contain these energies conservatively.

A major design goal for the ARIES-I reactor is passive safety. One way to achieve this is to keep radioactive inventories low enough that their full release would not cause significant environmental or safety impact. This approach may be feasible for the ARIES-I reactor and, therefore, it is desirable to minimize the tritium inventory in the plasma fueling system. Tritium inventories for various system components are given below in Table 5.6-VI although there is some uncertainty in these estimates. The tritium in the propellant gas is based on a maximum of 1% tritium contamination of the propellant gas for the two-stage pneumatic injector. It is assumed that the injector can be run for at least one day before the tritium contamination in the hydrogen propellant gas reaches

Table 5.6-VI.
Tritium Inventories (g) in ARIES-I Pellet-Injection System

Propellant gas in storage	10
Vacuum injection line (gas)	1
Vacuum pumps	10
Piping	5
Extruders (active and standby)	30
Pellet waste in injector vacuum system	3
TOTAL	59

this level. The tritium inventory in the piping and in the mechanical vacuum pumps is estimated at 15 g. This number depends on the actual pumps used and the surface area and arrangement of piping. The major contribution to the tritium inventory is the continuous extruder system. It is assumed that the active extruder has a working inventory of about 15 g of tritium, which is enough for about 3 to 4 minutes of continuous pellet fueling. During this time the standby extruder is being repositioned and recharged with DT fuel.

5.7. SUMMARY AND R&D DIRECTIONS

The impurity-control/particle-exhaust system is probably the most challenging subsystem in a fusion device. The ARIES-I reactor utilizes poloidal divertors in a double-null configuration. The divertors operate in the high-recycling mode (*i.e.*, exhibiting a high density and low temperature at the divertor target). The high-recycling mode at reactor-relevant parameters has not been demonstrated experimentally. The ARIES-I divertor performance is based on extrapolation of analytical and computational models that are calibrated to present-day experimental data. For modeling the ARIES-I edge plasma, two two-dimensional (2-D) edge-plasma computer codes, BRAAMS [1] and EPIC [2], were used. To ensure consistency with 0- and 1-D BALDUR core-plasma simulations, the edge-plasma analysis uses the particle and heat fluxes at the separatrix as inputs. The computational analyses indicate that the resultant plasma density at the separatrix would be high ($\sim 10^{20}$ m^{-3}) and a high-recycling divertor is formed with a peak heat flux of $\sim$4.5 MW/m^2 and a rather low plasma temperature of 10 to 20 eV at the divertor target. Furthermore, assuming that the ratio of α-particle to electron density is similar to that of the core plasma, calculations show that effective ash exhaust would be achieved.

First-wall erosion rates were determined assuming the carbon is sputtered from the silicon carbide (SiC). The average sputtering yield is taken to be 0.04. No credit is taken for redeposition since the sputtered material is swept towards the divertor. The sputtering contributions from deuterium, tritium, and alpha-particles are comparable and the total first-wall erosion is computed to be 0.3 mm/y. The divertor target plate is designed with a thin tungsten coating on the SiC-composite coolant tubes. The estimated tungsten erosion rate, dominated by α-particles, is 0.5 mm/y (assuming a conservative value of 0.15 for the ratio of net-to-gross erosion).

Because large uncertainties exist in the models and assumptions used in edge-physics codes, experimental edge-physics data, especially from large tokamaks, are needed to

further refine these codes. Also needed is extensive theoretical and computational effort to improve the physics models and reduce the uncertainty. Examples of areas that require improved physics understanding and modeling are the role of particle drifts and non-ambipolar flows in the edge plasma, neutral transport, and impurity radiation and transport.

Innovative approaches to the impurity control system, such as gas and/or impurity injection in normal and gaseous (or slot) divertors, should also be pursued. Finally, experiments to demonstrate plasma power and particle control (both fueling and pumping) at steady state (or for a time scale longer than wall absorption or degassing) are crucial to a power reactor.

Thermal response of the ARIES-I divertor plate to plasma disruption and the fluid dynamics of the melt layer have been analyzed numerically using 2-D codes. A simple model was used for vapor shielding, and only the surface tension and buoyancy forces were used in modeling the fluid dynamics of the melt layer. The divertor plate was modeled as a plate having a 2-mm-thick tungsten layer on top of a 0.5-mm SiC plate. The heat flux is incident on tungsten. The thermal quench time is 0.3 ms and the average and peak heat fluxes are, respectively, 8.8 and 44 GW/m^2. With a vapor shield, the total evaporation is estimated at 48 μm. The designated 1 mm of the tungsten coating is, therefore, expected to withstand about 20 full-power disruptions before requiring divertor plate replacement or recoating. Without a vapor shield, the thermal erosion rate is about twice as high and, therefore, the divertor plate lifetime would be halved. Liquid motion under the influence of buoyancy and surface tension forces is confined in the junction area of the peak and average heat-flux regions and appears to be small.

Because of the approximate nature of the analytical and numerical treatments, experimental observation is essential for studying the response of plasma-facing materials to disruption. Several such experimental studies have been performed [50 – 52]. However, the amount of data and the extent of the parameter range are insufficient to verify the analytical/numerical results and/or to develop empirical correlations. An R&D program is required to resolve the following areas: (1) The physics parameters, such as thermal quench time, heat flux, peaking factor, *etc.* need to be determined with greater certainty. (2) The formation and dynamics of the vapor shield and its interaction with the incident plasma particles should be studied to provide an adequate vapor-shield model. (3) A detailed code should be developed for analyzing the thermo-fluid dynamic behavior of the melt layer with recoil and electromagnetic forces, in addition to the buoyancy and surface tension, and the stability of the melt layer. (4) A redeposition model for an ablated surface during a disruption should be produced. (5) An adequate experimental

data base should be developed to verify the theoretical and numerical predictions as well as to develop empirical correlations.

ARIES-I will use an advanced, high-velocity pellet-injection system to achieve and maintain ignited plasmas. Three pellet injectors are provided. For ramp-up to ignition, a moderate velocity (1 to 1.5 km/s) single-stage pneumatic injector with high reliability and a high-velocity (4 to 5 km/s) two-stage pneumatic pellet injector using frozen hydrogenic pellets encased in sabots will be used. For the steady-state burn phase, a continuous single-stage pneumatic injector is proposed, which will provide a flexible fueling source beyond the edge region to aid in decoupling the edge region (constrained by divertor requirements) from the high-temperature burning plasma. All three pellet injectors are qualified for operation with tritium feed gas. Issues such as performance, neutron activation of injector components, maintenance, design of the pellet-injection vacuum line, gas loads to the reprocessing system, and equipment layout have been reviewed.

Pellet speed and size are two issues that strongly impact the design of the pellet injection system. For the ARIES-I reactor, it was assumed that shallow fueling beyond the scrape-off layer is sufficient (burn-phase injection velocity of 1 km/s). The current physics understanding and experimental data are not sufficient to analyze particle transport in the plasma core in order to arrive at the required pellet-penetration depth. If penetration to 1/3 of the plasma radius is required (as is the case assumed for ARIES-I transport analysis), then 5-km/s pellet speed will be needed and the moderate-velocity pellet injectors of ARIES-I should be replaced by the high velocity injectors. If even deeper pellet penetration (to 1/2 of the plasma radius) is required, then higher velocities ($\sim$20 km/s) will be needed and exotic technologies such as an e-beam rocket injector should be developed. Detailed transport studies should also be performed to determine the maximum plasma density perturbation per pellet allowed in a power reactor to ensure the fusion power changes remain below the engineering constraints.

REFERENCES

[1] B. Braams, "A Multi-Fluid Code for Simulation of the Edge Plasma in Tokamaks," NET report NET-68, EUR-FU/XII-80/87/68 (1987).

[2] E. Vold, "Transport in the Tokamak Plasma Edge," Ph.D. thesis, University of California Los Angeles (1989).

[3] E. Vold, A. K. Prinja, F. Najmabadi, and R. W. Conn, "The Neutral Diffusion Approximation in a Consistent Tokamak Edge Plasma-Neutral Computation," *J. Nucl. Mater.* **176&177** (1990) 570.

[4] S. I. Braginskii, "Transport Process in a Plasma," *Reviews of Plasma Physics,* M. A. Leontovich, Ed., Consultant Bureau, New York (1965) Vol. 1, p. 205.

[5] D. J. Santeler, "New Concepts in Molecular Gas Flow," *J. Vac. Sci. Technol.* **A4** (1986) 338.

[6] H. Yoshida, Japan Atomic Energy Research Institute, private communication during ITER workshop (1988).

[7] N. Matsunami, Y. Yamamura, Y. Itikawa, *et al.*, Nagoya University Institute of Plasma Physics report IPPJ-AM-232 (1983).

[8] F. Najmabadi, R. W. Conn, R. A. Krakowski, K. R. Schultz, D. Steiner, and the TITAN Research Group, "The TITAN Reversed-Field-Pinch Reactor Study—The Final Report," University of California Los Angeles, General Atomics, Los Alamos National Laboratory, and Rensselaer Polytechnic Institute, University of California Los Angeles report UCLA-PPG-1200 (1990); also, F. Najmabadi, R. W. Conn, R. A. Krakowski, K. R. Schultz, D. Steiner, and the TITAN Research Group, "Engineering and Physics of High-Power-Density, Compact, Reversed-Field-Pinch Fusion Reactors: The TITAN Study," *Proc. 15th Symp. Fusion Technol. (SOFT),* Utrecht, the Netherlands (Sept. 1988), *Fusion Technology 88*, A. M. Van Ingen, A. Nijsen-Vis, H. T. Klippel, Eds., North-Holland, Amsterdam (1989) p. 1779.

[9] K. R. Schultz, R. Gallix, C. Baxi, *et al.*, "Divertor and First Wall Armor Design for the TIBER-II Engineering Test Reactor," *Fusion Eng. Des.* **9** (1989) 15.

[10] E. T. Cheng, "Radioactivity Aspects of Fusion Reactors," *Fusion Eng. Des.* **10** (1989) 231.

[11] G. DeSalvo and J. A. Swanson, "ANSYS—Engineering Analysis System," version 4.1, Swanson Analysis Systems Inc., Houston, PA (1979).

[12] "PATRAN Users Manual," version 2.3, PDA Engineering, Costa Mesa, CA (1989).

[13] A. M. Hassanein, G. L. Kulcinski, and W. G. Wolfer, "Dynamics of Melting, Evaporation, and Resolidification of Materials Exposed to Plasma Disruptions," *J. Nucl. Mater.* **111&112** (1982) 554.

[14] H. Nakamura, T. Hiraoka, A. M. Hassanein, G. L. Kulcinski, and W. G. Wolfer, "First Wall Erosion During a Plasma Disruption in a Tokamak," Japan Atomic Energy Research Institute report JAERI-M 83-058 (1983).

[15] M. R. Holliday, J. M. Doster, and J. G. Gilligan, "Fusion Surface Material Melting, Ablation and Ejection Under High Heat Loading," *Fusion Technol.* **10** (1986) 782.

[16] A. SESTERO, "Protection of Walls from Hard Disruptions in Large Tokamaks,"*Nucl. Fusion* **17** (1977) 115.

[17] A. M. Hassanein, G. L. Kulcinski, and W. G. Wolfer, "Vaporization and Melting of Materials in Fusion Devices," *J. Nucl. Mater.* **103&104** (1981) 321.

[18] J. G. Gilligan, O. Auciello, M. Bourham, *et al.*, "Theoretical and Experimental Studies of the Vapor Shielding Mechanism for Surfaces Subjected to High Heat Fluxes," *Fusion Technol.* **15** (1989) 522.

[19] "ITER Physics Design Guidelines: 1989," ITER Documentation Series No. 10, International Atomic Energy Agency, Vienna (1990).

[20] S. Yamazaki, M. Seki, and M. Kobayashi, "Two-Dimensional Disruption Thermal Analysis Code," Japan Atomic Energy Research Institute report JAERI-M-88-163 (1988).

[21] S. I. Anisimov and A. Kh. Rakhmatulina, "The Dynamics of the Expansion of a Vapor When Evaporated into a Vacuum," *Sov. Phys. JETP* **37** (1973) 441.

[22] H. Kaburaki, M. Yokokawa, M. Seki, and T. Arisawa, "Numerical Analysis of Transient Behavior of Molten Metals Heated by Electron Beam," *Proc. Am. Soc. Mech. Eng.*, San Francisco, CA (1989).

[23] S. Schiller, U. Heisig, and S. Panzer, *Electron Beam Technology*, Wiley, New York (1982) p. 156.

[24] W. G. Wolfer and A. M. Hassanein, "On Melt Layer Stability Following a Plasma Disruption," *J. Nucl. Mater.* **111&112** (1982) 560.

[25] S. L. Milora, *J. Fusion Energy* **1** (1981) 15; also, S. L. Milora, "Review of Hydrogen Pellet Injection Technology for Plasma Fueling Applications," *Proc. 35th Nat. Symp. of American Vac. Soc.*, Atlanta, GA (Oct. 1988), *J. Vac. Sci. Technol.* **A7** (1989) 925.

[26] P. B. Parks, R. J. Turnbull, and C. A. Foster, "A Model for the Ablation Rate of a Solid Hydrogen Pellet in a Plasma," *Nucl. Fusion* **17** (1977) 539.

[27] S. L. Milora and C. A. Foster, *IEEE Trans. Plasma Sci.* **6** (1978) 578.

[28] W. A. Houlberg, S. L. Milora, and S. E. Attenberger, "Neutral and Plasma Shielding Model for Pellet Ablation," *Nucl. Fusion* **28** (1988) 595.

[29] P. B. Parks,"Magnetic-Field Distortion Near an Ablating Hydrogen Pellet," *Nucl. Fusion* **20** (1980) 311.

[30] P. C. Souers, "Hydrogen Properties for Fusion Energy," Ph.D. thesis, University of California Berkeley (1986).

[31] S. K. Combs, S. L. Milora, L. R. Baylor, *et al.*, "A Three-Barrel Repeating Pneumatic Pellet Injector for Plasma Fueling of the Joint European Torus," *Proc. 34th Nat. Symp. of American Vac. Soc.*, Anaheim, CA (Nov. 1987), *J. Vac. Sci. Technol.* **A6** (1988) 1901.

[32] K. Sonnenberg, P. Kupschus, W. Bailey, *et al.*, "High Speed Pellet Development," *Proc. IEEE 12th Symp. on Fusion Eng.*, Monterey, CA (Oct. 1987), IEEE No. 87CH2507-2, IEEE, Piscataway, NJ (1988) p. 1207.

[33] S. K. Combs, T. C. Jernigan, L. R. Baylor, S. L. Milora, and C. R. Foust, *Rev. Sci. Instrum.* **60** (1989) 2697.

[34] C. A. Foster, "Solid Deuterium Centrifuge Pellet Injector," *J. Vac. Sci. Technol.* **A1** (1983) 952.

[35] W. Amenda and R. S. Lang, Max-Planck-Institut fur Plasmaphysik report 1/187 (1981).

[36] W. D. Crozier and W. Hume, "High-Velocity, Light-Gas Gun," *J. Appl. Phys.* **28** (1957) 892.

[37] S. K. Combs, S. L. Milora, C. R. Foust, M. J. Gouge, D. T. Fehling, and D. O. Sparks, "Development of a Two-Stage Light Gas Gun to Accelerate Hydrogen Pellets to High Speeds for Plasma Fueling Applications," *Proc. 35th Nat. Symp. of American Vac. Soc.*, Atlanta, GA (Oct. 1988), *J. Vac. Sci. Technol.* **A7** (1989) 963.

[38] S. K. Combs, C. R. Foust, M. J. Gouge and S. L. Milora, "Acceleration of Small, Light, Projectiles (Including Hydrogen Isotopes) to High Speeds using a Two-Stage Light Gas Gun," *J. Vac. Sci. Technol.* **8** (1990) 1814.

[39] A. Reggiori, G. Riva, G. Daminelli, *et al.*, "Solid Deuterium Pellet Injection with a Two-Stage Pnuematic Gun," *Proc. 35th Nat. Symp. of American Vac. Soc.*, Atlanta, GA (Oct. 1988), *J. Vac. Sci. Technol.* **A7** (1989) 959.

[40] P. Kupschus, K. Sonnenberg, *et al.*, "Upgrading the JET Pellet Injector with a Two-Stage Light Gas Gun Prototype and Future Planning," *Proc. IEEE 13th Symp. on Fusion Eng.,* Knoxville, TN (Oct. 1989), IEEE No. 89CH2820-9, IEEE, Piscataway, NJ (1990) p. 1293.

[41] S. L. Milora and C. A. Foster, *Rev. Sci. Instrum.* **50** (1979) 482.

[42] L. D. Landau and E. M. Lifshitz, *Fluid Mechanics,* Pergamon Press, London (1959).

[43] D. D. Schuresko, S. L. Milora, J. T. Hogan, *et al.*, "Performance Characterization of Pneumatic Single Pellet Injection System," *J. Vac. Sci. Technol.* **A1** (1983) 959.

[44] S. K. Combs, S. L. Milora, C. R. Foust, *et al.*, *Rev. Sci. Instrum.* **56** (1985) 1173.

[45] P. W. Fisher, M. L. Bauer, L. R. Baylor, *et al.*, "Tritium Pellet Injector Results," *Proc. 35th Nat. Symp. of American Vac. Soc.*, Atlanta, GA (Oct. 1988), *J. Vac. Sci. Technol.* **A7** (1989) 938.

[46] J. Lafferanderie, G. Clandet, and I. Disdier, "Experimental Test of 6-mm Diameter D_2 Pellets Produced by In-Situ Condensation," *Proc. 14th Symp. Fusion Technol. (SOFT),* Avignon, France (Sept. 1986), *Fusion Technology 86*, A. M. Van Ingen, A. Nijsen-Vis, H. T. Klippel, Eds., North-Holland, Amsterdam (1987) p. 1367.

[47] M. J. Gouge, S. K. Combs, P. W. Fisher, and S. L. Milora, *Rev. Sci. Instrum.* **60** (1989) 570.

[48] A. E. Seigel, "The Theory of High Speed Guns," AGARDograph-91 (1965).

[49] E. C. Selcow, P. N. Stevens, I. C. Gomes, and L. M. Gomes, "Radiation Analysis of the CIT Pellet Injector System and its Impact on Personnel Access," *Proc. IEEE 12th Symp. on Fusion Eng.,* Monterey, CA (Oct. 1987), IEEE No. 87CH2507-2, IEEE, Piscataway, NJ (1988) p. 1088.

[50] M. Ogawa, M. Iraki, K. Fukaya, *et al.*, "Experimental Observation of Metal Surfaces Exposed to Intense Hydrogen Beam—Simulation of Plasma Disruption," *J. Nucl. Sci. Technol.* **26** (1989) 721.

[51] M. Seki, S. Yamazaki, A. Minato, *et al.*, "Improvement of an Electron Beam Facility as a Heat Source for Disruption Simulation Experiments," *Fusion Eng. Des.* **5** (1987) 215.

[52] J. R. Easoz and R. Bajaj, "Experimental Measurements of Melting and Vaporization Due to Simulated Plasma Disruptions," *J. Vac. Sci. Technol.* **A3** (1985) 1119.